JOURNAL OF GEOPHYSICAL RESEARCH, VOL. 112, B03307, doi:10.1029/2006JB004294, 2007

Geodetic, teleseismic, and strong motion constraints on slip from recent southern Peru subduction zone earthquakes

M. E. Pritchard,[1] E. O. Norabuena,[2] C. Ji,[3,4] R. Boroschek,[5] D. Comte,[6] M. Simons,[3] T. H. Dixon,[7] and P. A. Rosen[8]

Received 17 January 2006; revised 12 September 2006; accepted 18 October 2006; published 17 March 2007.

[1] We use seismic and geodetic data both jointly and separately to constrain coseismic slip from the 12 November 1996 M_w 7.7 and 23 June 2001 M_w 8.5 southern Peru subduction zone earthquakes, as well as two large aftershocks following the 2001 earthquake on 26 June and 7 July 2001. We use all available data in our inversions: GPS, interferometric synthetic aperture radar (InSAR) from the ERS-1, ERS-2, JERS, and RADARSAT-1 satellites, and seismic data from teleseismic and strong motion stations. Our two-dimensional slip models derived from only teleseismic body waves from South American subduction zone earthquakes with $M_w > 7.5$ do not reliably predict available geodetic data. In particular, we find significant differences in the distribution of slip for the 2001 earthquake from models that use only seismic (teleseismic and two strong motion stations) or geodetic (InSAR and GPS) data. The differences might be related to postseismic deformation or, more likely, the different sensitivities of the teleseismic and geodetic data to coseismic rupture properties. The earthquakes studied here follow the pattern of earthquake directivity along the coast of western South America, north of 5°S, earthquakes rupture to the north; south of about 12°S, directivity is southerly; and in between, earthquakes are bilateral. The predicted deformation at the Arequipa GPS station from the seismic-only slip model for the 7 July 2001 aftershock is not consistent with significant preseismic motion.

Citation: Pritchard, M. E., E. O. Norabuena, C. Ji, R. Boroschek, D. Comte, M. Simons, T. H. Dixon, and P. A. Rosen (2007), Geodetic, teleseismic, and strong motion constraints on slip from recent southern Peru subduction zone earthquakes, *J. Geophys. Res.*, *112*, B03307, doi:10.1029/2006JB004294.

1. Introduction

[2] We use seismic and geodetic data to determine the spatiotemporal distribution of fault slip during two large earthquakes in southern Peru (Figure 1): the 12 November 1996 M_w 7.7 Nazca, Peru, and the 23 June 2001 M_w 8.5 Arequipa, Peru, earthquakes, hereafter called the 1996 and 2001 earthquakes. In addition, we use seismic data to locate slip from the largest aftershocks of the 2001 earthquake on the fault interface: the 26 June 2001 M_w 6.7 and the 7 July 2001 M_w 7.6 earthquakes, both near Arequipa, Peru, and hereafter referred to as the June and July 2001 aftershocks. The largest aftershocks from the 1996 earthquake (both M_w 6.1) are well represented by a point source at the scale of our study [e.g., *Pritchard et al.*, 2006].

[3] Distributed slip models of large earthquakes have many applications, including constraints on the earthquake rupture process, assessments of seismic hazard, inputs to models of postseismic deformation, and for comparison with long-term evolution of the fore arc. Our particular interest in the southern Peru earthquakes is driven by the observation that the 2001 earthquake has significantly more postseismic after slip than the nearby M_w 8.1 1995 earthquake in northern Chile (hereafter referred to as the 1995 earthquake) [e.g., *Pritchard et al.*, 2002] and the 1996 earthquake in Peru [e.g., *Melbourne et al.*, 2002; *Pritchard*, 2003]. We seek to determine if these differences in postseismic deformation can be explained by differences in the rupture properties of these earthquakes (for example, different depths of rupture), or if some other explanation is required.

[4] From a technical perspective, we are interested in the ability of each data set to delineate earthquake rupture

[1]Department of Earth and Atmospheric Sciences, Cornell University, Ithaca, New York, USA.
[2]Departamento de Geodesia y Sismotectonica, Instituto Geofisico del Peru, Lima, Peru.
[3]Seismological Laboratory, Division of Geological and Planetary Sciences, California Institute of Technology, Pasadena, California, USA.
[4]Now at Department of Geological Sciences, University of California, Santa Barbara, California, USA.
[5]Departamento de Ingenieria Civil, Universidad de Chile, Santiago, Chile.
[6]Departamento de Geofisica, Universidad de Chile, Santiago, Chile.
[7]Rosenstiel School of Marine and Atmospheric Sciences, University of Miami, Miami, Florida, USA.
[8]Jet Propulsion Laboratory, California Institute of Technology, Pasadena, California, USA.

0148-0227/07/2006JB004294$09.00

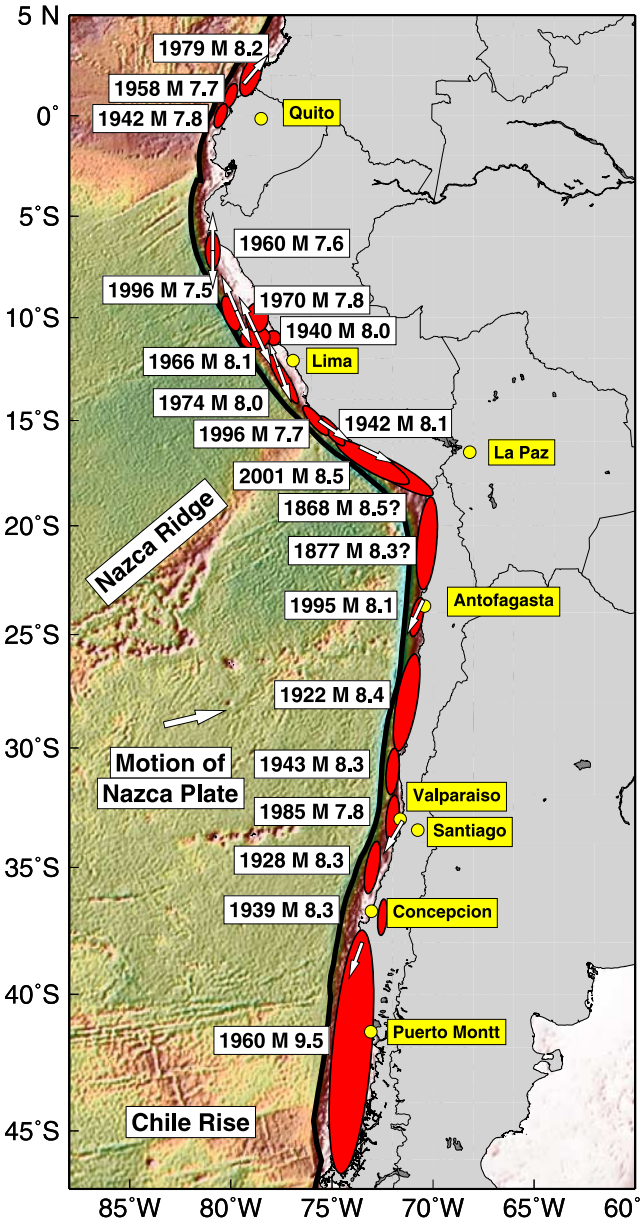

Figure 1. Rupture areas of the most recent large shallow interplate thrust earthquakes in western South America [*Beck and Ruff*, 1989; *Campos and Kausel*, 1990; *Beck et al.*, 1998] (with the exception of the 1939 and 1970 earthquakes, which were most likely intraplate). Seafloor bathymetry is shown in color, the trench location is a black line, the plate convergence direction is a white arrow, and selected cities are shown in yellow. The rupture zones of the earthquakes are approximated by red ellipses (defined by the aftershock locations), and the approximate azimuth of rupture is shown where known. Two arrows are shown if the rupture is bilateral (compiled from, e.g., *Benioff et al.* [1961], *Kanamori and Given* [1981], *Beck and Ruff* [1984], *Choy and Dewey* [1988], *Beck and Ruff* [1989], *Pelayo and Wiens* [1990], *Comte and Pardo* [1991], *Mendoza et al.* [1994], *Swenson and Beck* [1996], *Langer and Spence* [1995], *Ihmlé et al.* [1998], *Beck et al.* [1998], *Spence et al.* [1999], *Swenson and Beck* [1999], *Carlo et al.* [1999], *Giovanni et al.* [2002], and *Bilek and Ruff* [2002]).

properties. By using the same elastic structure and fault geometry in the joint and independent inversions of each data set for fault slip, we can directly compare the slip distributions and seismic moments.

2. Data Used

[5] Previous studies of the rupture processes of the 1996 and 2001 earthquakes have relied purely on teleseismic data [*Swenson and Beck*, 1999; *Spence et al.*, 1999; *Giovanni et al.*, 2002; *Bilek and Ruff*, 2002; *Tavera*, 2002; *Robinson et al.*, 2006], although *Salichon et al.* [2003] coupled teleseismic data with one ERS interferogram to study the 1996 earthquake, and a single GPS station was used to study the 2001 earthquake [*Ruegg et al.*, 2001; *Melbourne and Webb*, 2002]. Further study of the 1996 earthquake is warranted because more geodetic data are available, and there are conflicting reports of the depth of rupture, with one model favoring slip to 66 km [*Spence et al.*, 1999] and another placing most slip above 50 km [*Salichon et al.*, 2003]. The depth of rupture is an important parameter for understanding the variations in postseismic after slip within this region [e.g., *Melbourne et al.*, 2002].

[6] While we use the same type of teleseismic data for all earthquakes, different sets of geodetic data are available for the 1996 and 2001 earthquakes. For example, we have used InSAR data from four satellites, and each satellite has a different viewing geometry, wavelength (λ), precision of orbital ephemeris, and other parameters: ERS-1 and -2 (European, λ = 5.6 cm or C band); JERS-1 (Japanese, λ = 24 cm, or L band); and RADARSAT-1 (Canadian, C band). There are also different quantities of campaign GPS measurements for the 1996 and 2001 earthquakes.

[7] We process the InSAR data using the publicly available ROI_PAC software suite [*Rosen et al.*, 2004] along with the 90-m digital elevation model (DEM) from the Shuttle Radar Topography Mission (SRTM) [*Farr and Kobrick*, 2000]. Because of uncertainties in the quality of the orbital ephemeris (especially for JERS and RADARSAT), we empirically estimate the baselines. We calculate the baseline parameters (e.g., horizontal and vertical baselines parameterized as quadratic functions of time on orbit [*Pritchard et al.*, 2002]) that minimize the phase difference between the interferogram and a synthetic interferogram made with a DEM after removing a preliminary model of coseismic deformation. We reduce the number of points from millions to hundreds or thousands by subsampling the interferogram with a density of points proportional to the displacement field [*Simons et al.*, 2002].

[8] The GPS data [*Norabuena et al.*, 1998, 1999] are processed using GIPSY-OASIS II (release 2.5) [*Zumberge et al.*, 1997] and the no fiducial approach of *Heflin et al.* [1992]. In this analysis, pseudorange and carrier phase information were combined with clock data and precise ephemeris provided by the Jet Propulsion Laboratory. The daily nonfiducial solution of the local network, combined with about 400 GPS global stations were aligned to the ITRF97 conventional terrestrial reference frame. Interseismic deformation was removed from the campaign stations by using observations from 1994, 1996, 1997, and 1999 and extrapolating the measured rates to the day before the earthquake. Different methods were used for dealing with

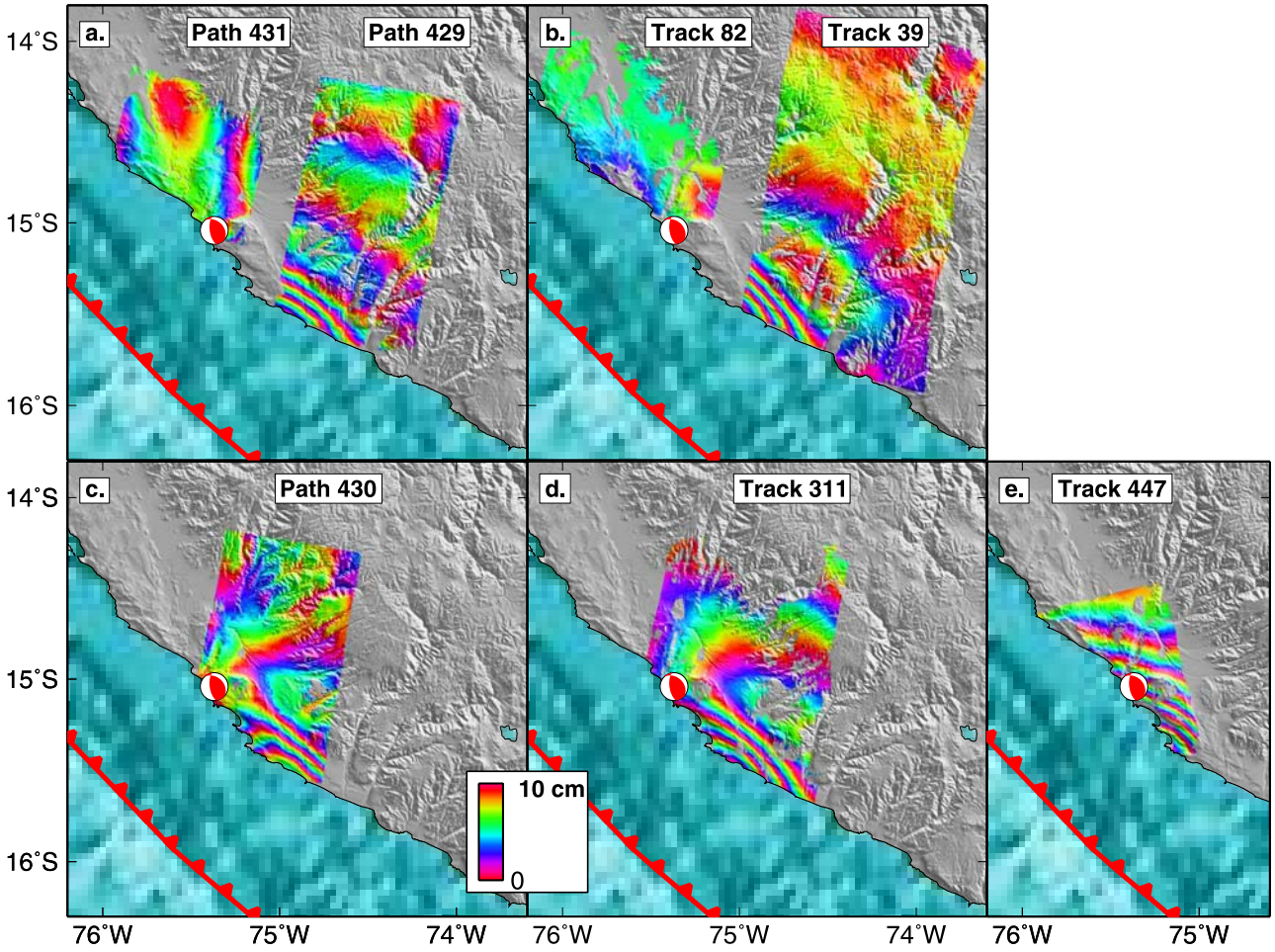

Figure 2. Coseismic interferograms for the 1996 earthquake over shaded topographic relief and bathymetry, with the trench shown as a red barbed line. See Table 1 for dates of all interferograms. (a) JERS interferograms from paths 431 and 429. (b) ERS interferograms from tracks 82 and 39. (c) JERS path 430. (d) ERS track 311. (e) ERS ascending track 447, which has more deformation than the other interferograms. An M_w 6.1 aftershock on 9 February 1997 at 20 km might cause some of the deformation in track 82 and path 429.

the postseismic deformation following the 1996 and 2001 earthquakes, and are discussed below.

2.1. The 1996 Earthquake

2.1.1. Geodetic Data

[9] For the 1996 earthquake, we have seven interferograms from six different descending orbital tracks, three from ERS and three from JERS (Figure 2 and Table 1). In addition, we use a single track of data from an ascending orbit of ERS. InSAR only measures one component of the deformation field, in the direction of the radar line of sight (LOS) (for further discussion of InSAR, see reviews by *Massonnet and Feigl* [1998] and *Rosen et al.* [2000]). The LOS direction for ERS and JERS data are different (approximately 23° from vertical for ERS, and 44° for JERS), and therefore have significantly different sensitivities to horizontal and vertical motion. Furthermore, interferograms from the different orbital tracks overlap and have slightly different viewing geometry for a given ground location. Thus, by using data from multiple satellites and viewing geometries, we are sensitive to more than one component of deformation. In the interferograms, we measure a maximum deformation in the LOS of about 0.35 m in the descending tracks and 0.7 m in the ascending track. All of the interferograms include interseismic deformation (up to 5.5 years) and at least several months of any potential postseismic deformation. It is difficult to separate interseismic and postseismic deformation from errors in the satellite orbits, so all of these parameters are removed simultaneously via the estimation of quadratic spatial ramps during the modeling (see modeling strategy in Appendix A). Combining multiple InSAR observations (spanning different time spans) with the seismic data, facilitates separation of coseismic, interseismic, and postseismic deformation. There is no evidence for postseismic deformation between January 1997 and December 1999 [*Pritchard*, 2003].

[10] Three campaign GPS stations within the rupture area were occupied in June 1996 and October 1997, and can be used to constrain the coseismic deformation (Table 2). The interseismic deformation rate at these stations was assumed

Table 1. ERS, JERS, and RADARSAT Interferograms Used to Constrain Coseismic Deformation From the 2001 and the 1996 Earthquakes

Track	Frame(s)	Image 1	Image 2	$B_\perp$,[a] m
		1996 Nazca Earthquake		
311	3897–3915	23 May 1992	22 Sep 1997	125
82	3897	27 May 1993	12 Oct 1997	230
39	3897–3915	24 Oct 1996	9 Oct 1997	100
447	6885	26 Apr 1996	5 Apr 2002	230
p429[b]	325–326	4 Mar 1994	21 Apr 1997	250
p430[b]	325–326	19 May 1995	9 Mar 1997	200
p431[b]	325	29 Oct 1996	10 Mar 1997	900
		2001 Arequipa Earthquake		
N/A[c]	3927–3960	22 Jul 2000	3 Sep 2001	150
225	3915–3951	9 Apr 1996	9 Jan 2002	40
454	3915–3951	2 Nov 1995	21 Dec 2001	110
89	6849–6867	10 Jan 1999	9 Jul 2001	170
182	3933–3969	18 Nov 1995	17 Nov 2002	90
497	3915–3933	6 Oct 1997	13 Jan 2003	40
404	6867	29 Dec 1998	16 Jul 2002	250

[a]$B_\perp$ is the perpendicular component of the baseline between the two satellite images used to make the interferogram. Large $B_\perp$ increases sensitivity to topographic relief [e.g., *Rosen et al.*, 2000].

[b]JERS data are archived as paths, so the letter "p" precedes the numerical value.

[c]There are no official track numbers for RADARSAT, so they are listed as N/A (not applicable). RADARSAT data are from standard beam 7.

constant between 1994 and 1997 and estimated using the observations in 1994 and 1996. This rate was extrapolated until the day prior to the earthquake (in November 1996) to obtain the coseismic offset (Figure 3).

2.1.2. Teleseismic Data

[11] We select azimuthally well-distributed digital P and SH teleseismic displacement records (between 30° and 90°) from the global network [*Butler et al.*, 2004]. See *Pritchard et al.* [2006] for more details about selection and processing of the teleseismic data. For the 1996 earthquake, we use 18 P and 13 SH waveforms. We use records extending 80 s after the arrival of each phase (Figure 4).

2.2. The 2001 Earthquake

2.2.1. Geodetic Data

[12] There are 12 campaign and 2 continuous GPS measurements of coseismic deformation from the 2001 earthquake (Table 2 and Figure 5) [*Norabuena*, 2004]. The interseismic deformation was removed using the inferred rates of deformation between 1994 and 1999 up to the day of the earthquake for all stations except MDRG, where measurements before May 2001 do not exist (but the deformation between the first occupation and the earthquake should only be a few millimeters in the horizontal). No assumption was made regarding the postseismic deformation that occurred in the days to months between the earthquake and the occupation of any of the GPS sites. All interferograms include deformation from the large aftershocks (principally the M_w 7.6 on 7 July 2001) and we discuss how we removed the deformation from this earthquake from the interferograms in section 3.2.1.

[13] We have made seven interferograms spanning the 2001 earthquake: six from ERS orbital tracks (four descending and two ascending); and one from a descending RADARSAT orbit (Figure 6 and Table 1). We measure a maximum deformation in the LOS of about 1 m in the RADARSAT interferogram (LOS 45° from vertical). We attempted to use azimuth offsets [e.g., *Michel et al.*, 1999; *Peltzer et al.*, 1999; *Simons et al.*, 2002] to measure the horizontal deformation, but the signal to noise ratio (SNR) was too low for these long-term, low-coherence interferograms (the predicted signal is less than 60 cm, while the error is several 10s of cm). We equally weight the InSAR observations, but give a greater weight to the GPS stations (factor of 2–10 depending on the error for each component).

Table 2. Coseismic GPS Displacements and 1 Standard Deviation Errors (σ)[a]

Station	Latitude	Longitude	E	N	V	σ_E	σ_N	σ_V	Pre	Post
				1996 Nazca Earthquake						
TANA	−15.75°	−74.45°	−104	19	10	4	2	7	Jun 96	Oct 97
ZAMA	−14.66°	−75.62°	−113	73	13	2	1	4	Jun 96	Oct 97
CANA	−13.98°	−73.93°	−54	−36	28	2	1	4	Jun 96	Oct 97
				2001 Arequipa Earthquake						
AREQ	−16.47°	−71.49°	−416	−299	−26	0.2	0.1	0.4	22 Jun 01	23 Jun 01
AYRO	−17.75°	−69.88°	−175	5	−14	2	1	4	30 Jul 99	24 Sep 01
BAJO	−16.95°	−70.35°	−346	−124	−64	3	1	5	22 Jul 99	29 Jul 01
CMOR	−18.05°	−70.66°	−206	14	−55	2	1	4	27 Jul 99	15 Jul 01
COMA	−17.04°	−68.44°	−40	−27	2	3	1	6	15 Aug 99	23 Sep 01
JHAI	−16.52°	−72.86°	−888	−604	−234	2	1	4	11 Jul 99	28 Jun 01
LAMP	−15.33°	−70.34°	−120	−113	4	3	1	5	13 Jul 99	10 Aug 01
MACU	−14.08°	−70.41°	−41	−50	0	3	1	5	14 Jul 99	2 Oct 01
MDRG	−15.59°	−71.82°	−182	−215	NA	1	4	NA	1 May 01	23 Sep 01
MIST	−16.30°	−71.43°	−352	−264	−28	1	0.2	5	22 Jun 01	23 Jun 01
PNAS	−16.23°	−68.49°	−46	−25	10	3	1	6	7 Jul 99	23 Sep 01
POCO	−17.43°	−71.37°	−782	−146	−68	2	1	5	21 Jul 99	30 Jun 01
SIGN	−16.49°	−71.54°	−515	−365	NA	1	0.2	NA	10 May 01	17 Jul 01
TANA	−15.75°	−74.45°	−230	15	NU	5	2	NU	16 Jul 99	28 Jun 01

[a]All in mm. The dates of observation before and after the earthquakes are listed as "Pre" and "Post," respectively, although the given displacements only include coseismic and postseismic motion, because the interseismic deformation was removed (see text). NA, not available. NU, not used (see text).

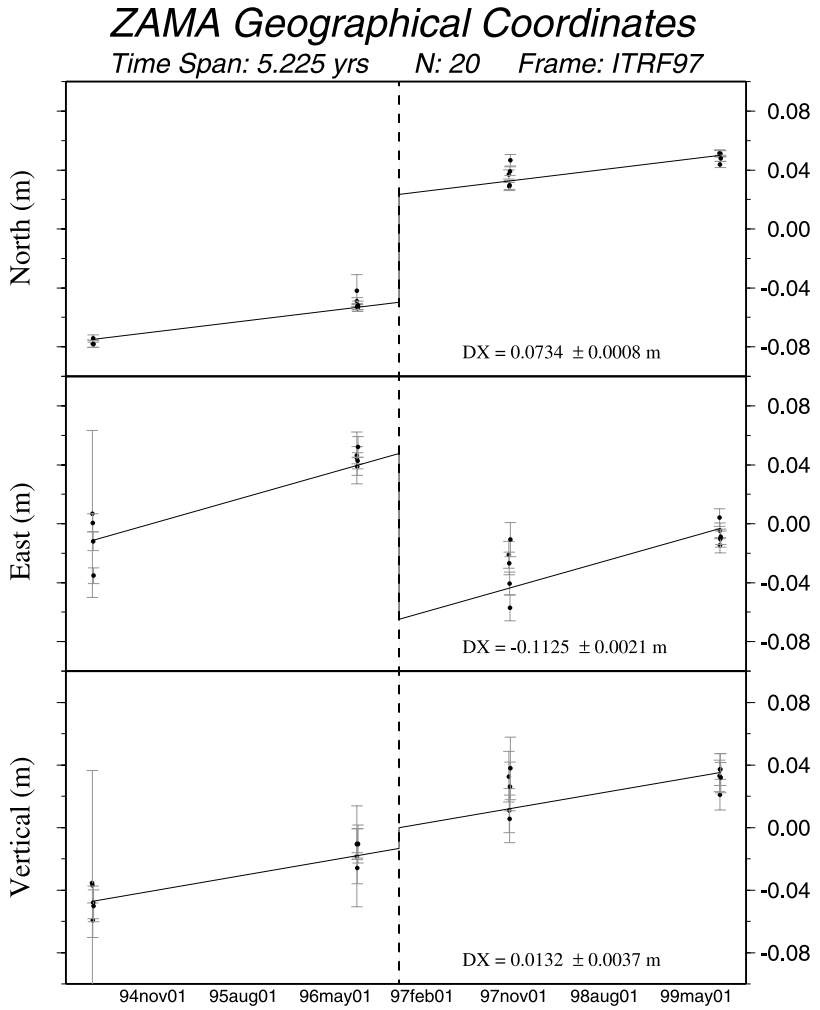

Figure 3. Position of GPS station ZAMA is shown in three dimensions before and after the 1996 Peru earthquake (shown by the vertical line). The daily solutions are shown by the black circles with one standard deviation error bounds. The inferred 1996 coseismic offset and error are listed for each component as DX (see also Table 2).

2.2.2. Teleseismic Data

[14] We use P records that are 135 s long (although we cut the record shorter at a few stations to avoid interference from PP), and SH records that are 180 s long. We use 17 P and 12 SH records (Figure 7). It has been observed that large subduction earthquakes excite large amplitude, nearly monochromatic (14 seconds) oscillations on seismographs at all azimuths following the P wave, possibly caused by reverberations in the water column near the rupture area in the trench [*Ihmlé and Madariaga*, 1996], but these oscillations have not been observed following this earthquake.

2.2.3. Strong Motion Data

[15] The 2001 earthquake was recorded on 11 strong motion stations in three different arrays, but only one station is located within the rupture area, and the majority of the other records are far away or only record part of the rupture (Figure 8). The station within the rupture area is the analog station in Moquegua (hereafter called MOQU) from the CISMID array (Peru-Japan project http://www.cismid-uni.org/p_acelerograf/registros3.htm), located 329 km from the hypocenter [e.g., *Tavera and Salas*, 2002; *Rodriguez-Marek et al.*, 2003]. Only the last few tens of seconds are available from the other analog station from this array in the city of Tacna. Another array run by the Instituto Geofisico del Peru has two analog stations NW of the hypocenter more than 400 km away, and with small amplitudes (of order a few centimeters per square second) because of directivity [*Tavera and Salas*, 2002].

[16] The third array is located in Chile and contains six analog stations (Kinemetric SMA-1, triggered without absolute time) and one digital station (Kinemetric Etna), with all stations between 453 and 590 km from hypocenter, but 200–300 km from the southeast extreme of inferred slip [*Boroschek et al.*, 2001]. Two of the analog stations are in Arica (the same location as the digital station). Of the remaining stations, only one has a record longer than about 30 s, while the strong ground shaking lasts for more than 100 s. We remove periods below 0.1 Hz for analog stations [*Shakal et al.*, 1986].

[17] The digital record is of high quality (located in the Arica hospital, hereafter called AHOS), and can include longer periods, although we were not able to retrieve a

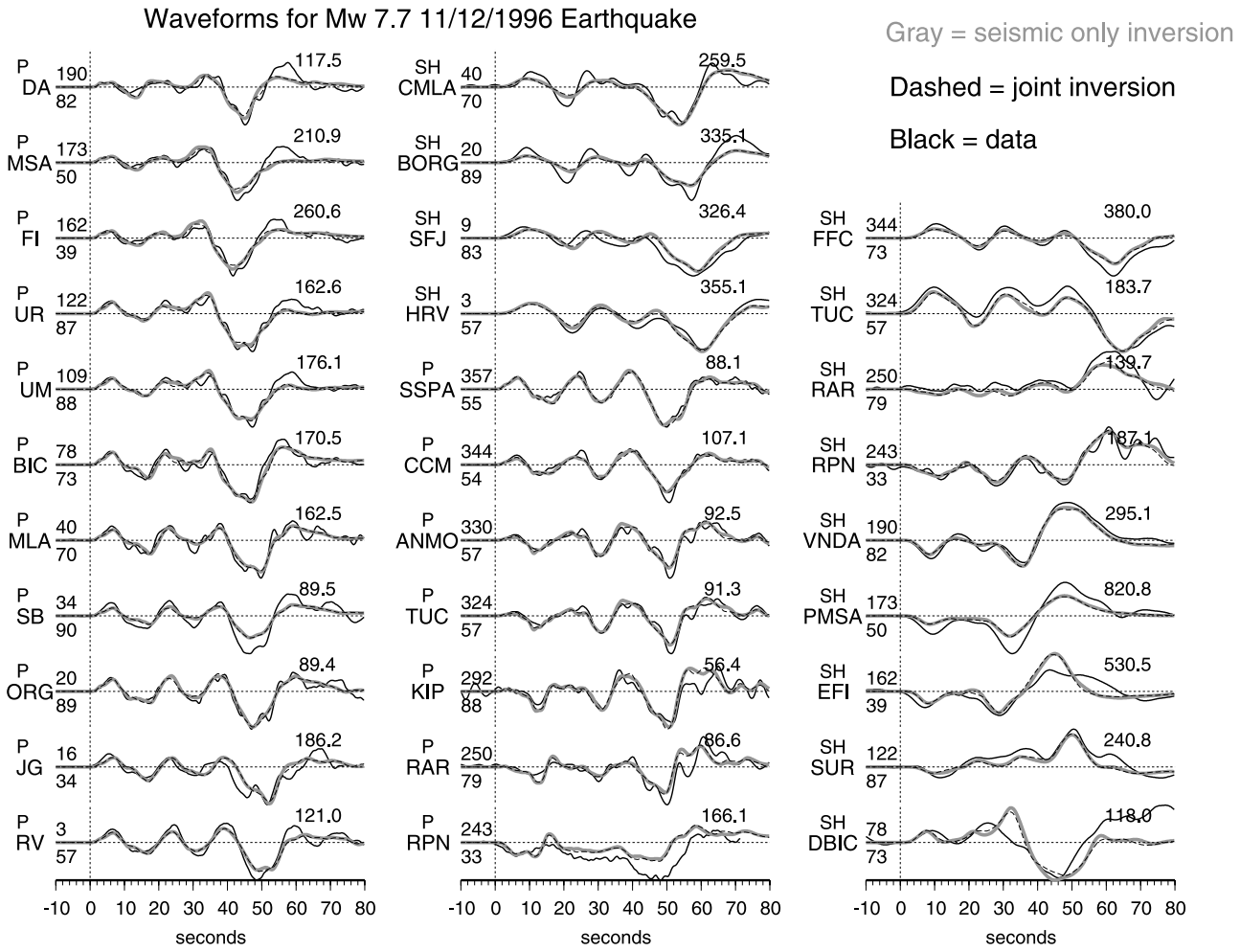

Figure 4. Teleseismic displacement data (P and SH) used in the slip inversion for the 1996 earthquake (black lines) and calculated synthetics from the teleseismic-only (gray lines) and joint inversions (black dashed lines). To the left of each trace is the station name, epicentral distance (lower number), and azimuth (upper number, which increases from the bottom of the page to the top). The type of record (P or SH) is listed above each station name. Each amplitude has been normalized by the maximum displacement, shown in microns to the upper right of each trace.

reliable coseismic offset from it or the other stations. We have compared the digital record to the two analog records from Arica, and found that they match each other in the 0.1 and 1 Hz band. We note that, based on comparing the digital and analog records, as well as the predicted strong motion record from a single large asperity, we determined that the polarity of all three components of the digital record were reversed. In addition, the longitudinal and transverse records from the Arica, Costanera station are switched, and the Longitudinal record from Costanera has a flipped polarity.

[18] We use all three components at each of the two strong motion stations in the inversion: AHOS and MOQU (Figure 8). MOQU was filtered with a trapezoidal filter between 0.05–0.1 and 20–50 Hz by CISMID, and given our experience with the other analog records, the longer periods would probably not be useful. We low-pass filter AHOS at 0.3 Hz, and remove frequencies above this value also from MOQU. After the filtering, we integrate the waveforms to create velocity seismograms that are used in the inversions. Because of the additional filtering necessary for MOQU, the AHOS and MOQU waveforms include different frequencies and to account for this fact, we use different wavelet bands for each (see modeling strategy in Appendix A).

2.3. The 2001 Aftershocks

[19] All of our interferograms, and some of the GPS displacements include deformation from the largest shallow aftershocks following the 2001 earthquake on 26 June and 7 July. It is difficult to separate deformation from the aftershocks from the main shock using the available InSAR and GPS data. Therefore we use just the teleseismic data to constrain the fault slip from these events. We use 60 seconds of 14 P and 11 SH records for the June aftershock (Figure 9). For the July aftershock, we use 90 s of 15 P and 12 SH records (Figure 10). Some constraints on the coseismic deformation are provided by the continuous

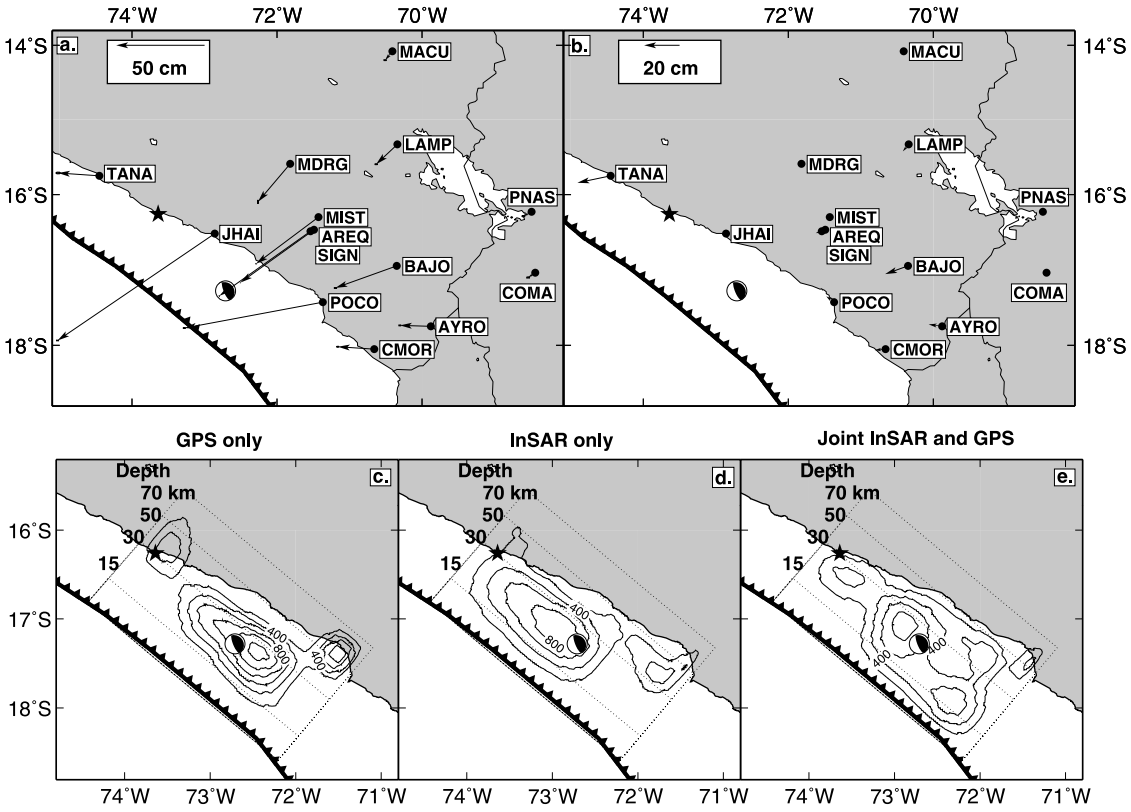

Figure 5. (a) Location of the 12 campaign and 2 continuous GPS stations and the coseismic horizontal deformation from the 2001 earthquake. Error ellipses are shown but are usually too small to be seen. The trench is shown as a black barbed line. (b) Residual horizontal deformation (data minus joint teleseismic/strong motion/geodetic model). RMS misfits between data and the GPS-only, InSAR-only, geodetic-only, teleseismic-only, and joint models are in parentheses: east component (4.7 cm; 11.5 cm; 5.8 cm; 5.7 cm); north (1.3 cm; 22.0 cm; 2.1 cm; 2.1 cm); vertical (0.8 cm; 3.8 cm; 3.0 cm; 2.6 cm). (c) Slip distribution from GPS-only inversion. (d) Slip distribution from InSAR-only inversion. (e) Joint GPS-InSAR inversion (same as Figure 11b).

GPS station in Arequipa [*Ruegg et al.*, 2001; *Melbourne and Webb*, 2002; SOPAC http://sopac.ucsd.edu/] and will be compared with our teleseismic model below.

3. Results

3.1. The 1996 Earthquake

[20] The slip distributions from the teleseismic-only, geodetic-only and joint inversions for the 1996 earthquake are shown in Figure 11. Details of how these models are generated are discussed in Appendix A. Mean properties of the rupture (risetime, rupture velocity, moment, and rake) are in Table 3, and the spatiotemporal evolution is in Figure 12. We estimate an average rupture velocity of 2.9 km/s, which is larger than the only previously published estimate of 2.25 km/s [*Swenson and Beck*, 1999]. Residual interferograms are in Figure 13. In general, the RMS misfits between model and geodetic data are higher in southern Peru (for both the 1996 and 2001 earthquakes) than northern Chile [*Pritchard et al.*, 2006]. The higher misfit in Peru could be caused by the lower signal-to-noise ratio (SNR) of each interferogram because of the lower coherence relative to Chile [*Pritchard and Simons*, 2004], and/or because the SNR can be increased by data stacking in Chile but not Peru, due of the dearth of data coverage in Peru.

3.1.1. Seismic Moment

[21] Previous inversions have found a wide range of seismic moments for this earthquake, although some of the difference may be caused by different assumed rigidity (the different studies assume a variety of crustal velocity models where rigidities can differ by more than 40%). Moments from teleseismic-only inversions range from $2.4–3.5 \times 10^{20}$ N m (M_w 7.5–7.6) [*Swenson and Beck*, 1999] to 1.5×10^{21} N m (M_w 8.0) [*Spence et al.*, 1999]. *Salichon et al.* [2003] performed InSAR-only (one track of data), teleseismic only, and joint inversions, and found a moment of 4.1×10^{20} N m (M_w 7.7) for the InSAR or teleseismic inversions and 4.4×10^{20} N m (M_w 7.7) for the joint inversion. As part of their inversion, they minimized the difference between their moment and the Harvard centroid moment tensor (CMT) moment (4.6×10^{20} N m M_w 7.7).

[22] In general, the slip distributions with moment above about 5×10^{20} N m (M_w 7.7), have slip near the trench or at significant depth, regions that are poorly resolved by the geodetic data. Therefore, following *Salichon et al.* [2003], we force all inversions to have a seismic moment near the

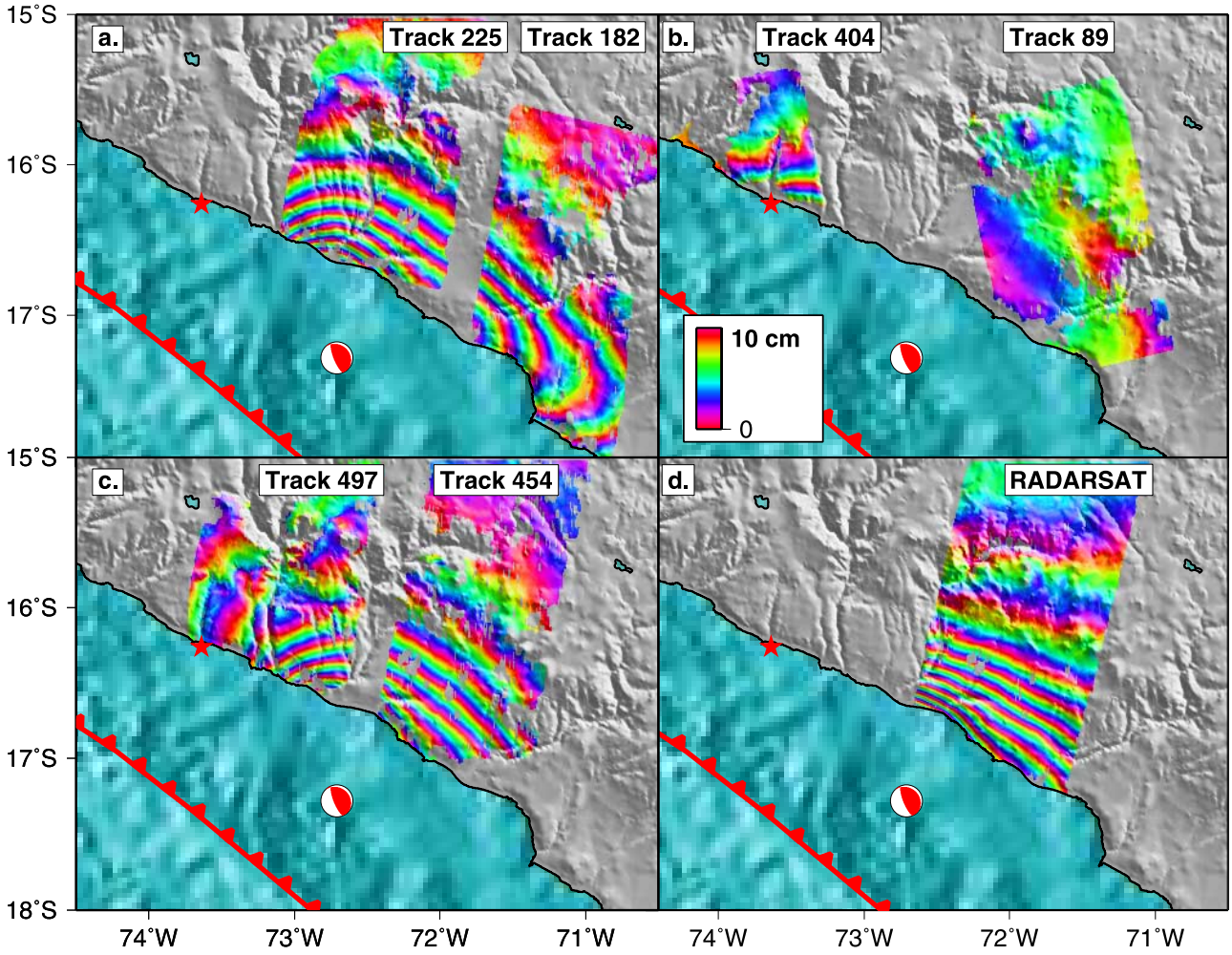

Figure 6. Interferograms from seven orbital tracks spanning the 2001 earthquake (see Table 1 for dates). The trench (red barbed line), CMT location (red mechanism), and hypocenter (NEIC, red star), are also shown. (a and c) Descending ERS data. (b) Ascending ERS data. (d) Descending RADARSAT interferogram.

Harvard CMT moment. The unconstrained geodetic moment from our inversion is 7×10^{20} N m (M_w 7.8), and while the lower moment inversions constrained to be near the Harvard CMT moment underpredict the amplitude of some teleseismic waveforms (e.g., the third negative P pulse at azimuths of 160°–200°), they better fit the first negative P pulse at azimuths between 200° and 330°.

[23] The unconstrained geodetic-only inversion using both JERS and ERS data favors a moment that is 30–50% higher than the Harvard CMT moment, depending on the model parameterization. For example, the unconstrained geodetic moment is 10% lower when a fault plane with only a single dip of 30° is used, and we find a moment 20% higher when the Wollard crustal seismic velocity model is used instead of the Husen model (see Appendix A for a description of the velocity models). We do not think that the high geodetic moment indicates significant aseismic deformation, but instead illustrates the nonunique nature of slip inversions. For example, separate inversions of the ERS or JERS data favor even higher moments (8.4×10^{20} N m, M_w 7.9 and 13×10^{20} N m, M_w 8.0 respectively), than the combined geodetic inversion. In addition, the geodetic and teleseismic data are fit almost as well with the smaller seismic moment (geodetic RMS generally differ by fractions of a mm). We favor a moment similar to the Harvard CMT moment because of the better fit to the initial pulse of the teleseismic waveforms (described above). Variations in the crustal velocity structure affect detailed fits to the waveforms. For example, the discrepancies in the first P pulse azimuths between 200° and 330° mentioned above, are diminished when the Wollard velocity model is used, although there is then a poorer fit at other stations.

3.1.2. Comparing Inversions With Different Data Sets

[24] Our slip models for the teleseismic-only, geodetic-only, and joint inversions of the 1996 earthquake are similar to each other and previous results in terms of rake and general slip distribution. In agreement with previous work [*Swenson and Beck*, 1999; *Spence et al.*, 1999; *Salichon et al.*, 2003], we find that the earthquake ruptures unilaterally to the south (Figure 12), with most of the moment release occurring 50–100 km from the hypocenter and southeast of the Harvard CMT location. There are some differences

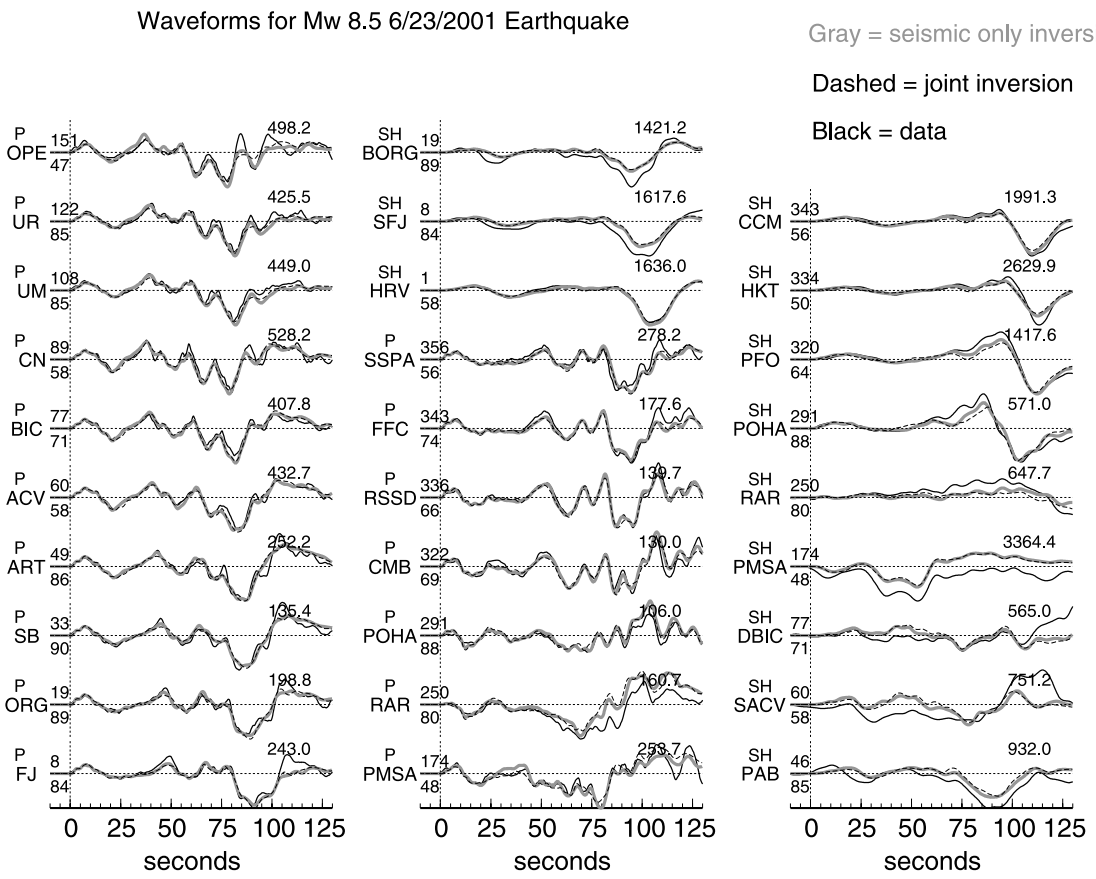

Figure 7. Teleseismic displacement data (P and SH) used in the slip inversion for the 2001 earthquake (black lines) and calculated synthetics from the teleseismic-only (gray lines) and joint inversions (black dashed lines). Conventions are the same as in Figure 4.

between the models: the teleseismic-only and joint models have more slip near the hypocenter than the geodetic-only result. In addition, the geodetic-only and joint models have more continuous slip between the Harvard CMT location and the southern extreme of rupture, while the teleseismic-only result is more discontinuous. We observe a similar difference between the seismic-only and joint models for the 2001 earthquake (see later discussion).

3.1.3. Comparing JERS and ERS Data

[25] We have equally weighted the two types of InSAR data, but we experiment with different weighting, because the relative sensitivity of ERS and JERS is not known. Because of a problem shortly after launch, JERS transmitted about one quarter as much power as it was designed to, but this seems to have only a small effect upon the SNR [e.g., *Murakami et al.*, 1996]. The accuracy of JERS orbital locations is much poorer than for ERS, but our procedure for empirically estimating the baselines for both data sets, neutralizes any advantage for ERS. From the inversion with equal weighting, the RMS residuals from JERS and ERS are about the same (1 cm, see Figure 13). For the Northridge earthquake, differences between JERS observations and GPS measurements are similar to ERS-GPS differences (centimeter-scale) [*Rosen et al.*, 1996; *Murakami et al.*, 1996]. We conclude that previous estimates of the JERS error budget are too conservative for our observations (4.2 cm [*Murakami et al.*, 1996]). Our small residual between the JERS data and the model is much less than in previous studies (10s of cm) of the earthquakes of Northridge, California, Sakhalin Island, Kobe and Mount Iwate, Japan [*Murakami et al.*, 1996; *Massonnet et al.*, 1996; *Tobita et al.*, 1998; *Ozawa et al.*, 1997; *Fujiwara et al.*, 2000].

3.1.4. Comparing InSAR and GPS Data

[26] We perform inversions of the geodetic data both with and without the three available GPS stations where coseismic deformation was measured (Table 2). We experiment with different weighting of the InSAR and GPS data. One of the GPS stations can be directly compared to three different tracks of InSAR data, and when the GPS data are weighted 10 times more than the InSAR, the RMS is 1.7 cm and the mean is -2.2 cm. The misfit to all the GPS data is usually 4–8 cm in the horizontal, with the largest misfit at the station that overlaps with the InSAR data (ZAMA), indicating some discrepancy between the data types (probably related to incompatible removal of interseismic deformation in the InSAR and/or GPS). The slip distribution is not significantly changed by the addition of the GPS data, and so in the "geodetic-only" inversions we show the results from the InSAR-only inversions.

3.2. The 2001 Earthquake

[27] We show the slip from the 2001 earthquake in Figures 5, 8, and 11, the InSAR residuals in Figure 14, GPS residuals in Figure 5, the teleseismic waveforms in

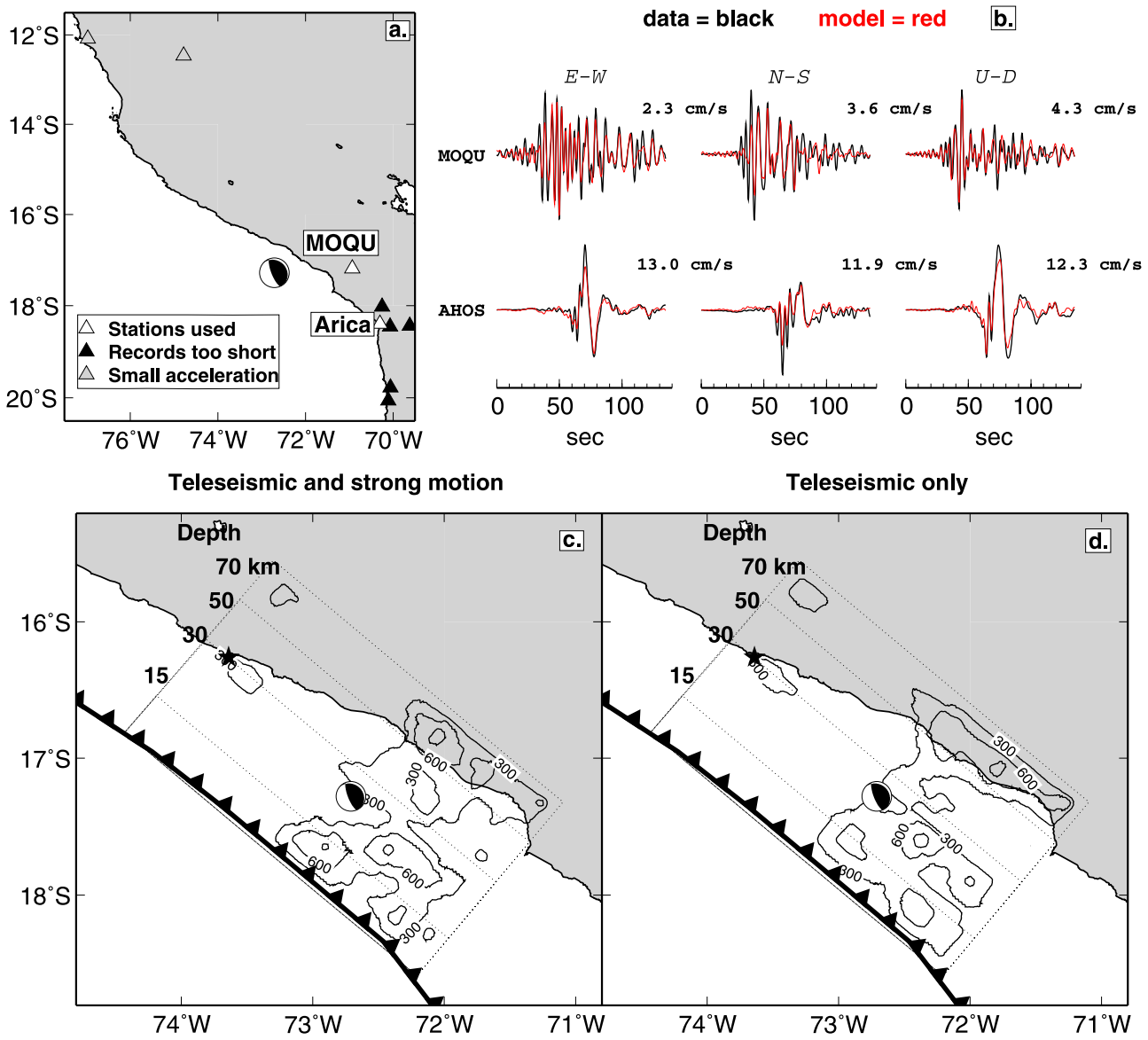

Figure 8. (a) Location of the 11 strong motion stations which recorded the 2001 earthquake, where only the two stations used in the inversion are labeled. Three stations are colocated in Arica, Chile (including AHOS). (b) Strong motion velocity waveforms (black lines, each station has different filtering, see text) and calculated synthetics from the teleseismic and strong motion only inversion (red lines). For each component, the absolute value of the maximum velocity is listed. (c) Slip distribution from joint teleseismic and strong motion data with 3 m contour interval. The trench (black barbed line), Harvard CMT mechanism, and NEIC hypocenter (black star) are also shown. (d) Slip distribution from just teleseismic data (same as Figure 11a).

Figure 7, and the spatiotemporal evolution of slip in Figure 15. Mean properties of the rupture (risetime, rupture velocity, moment, rake) are in Table 3.

3.2.1. Effect of Large Aftershocks on Geodetic Data

[28] Deformation from the June and July aftershocks is included in all of our interferograms spanning the main shock, and thus our InSAR-only estimates of coseismic slip from the M_w 8.5 earthquake could be too high. Not all of the GPS stations are contaminated by the aftershocks, but horizontal deformation could be 1–2 cm at BAJO and SIGN. For the June aftershock, the maximum surface deformation within the subaerial extent of our InSAR and GPS data sets inferred from our teleseismic-only inversions is only about 2 cm, but is more than 10 cm for the July aftershock. However, our predicted surface displacements from the aftershocks are inaccurate. While predicted surface deformation from teleseismic-only inversions of M_w ~6 earthquakes can be as accurate as geodetic-only models (depending on the earthquake depth), for M_w >7 earthquakes, the teleseismic-only models do not match the data well (Figure 16) [*Pritchard et al.*, 2006].

[29] To test the sensitivity of our results to the deformation from the aftershocks, we perform inversions for the 2001 main shock with and without the aftershock deforma-

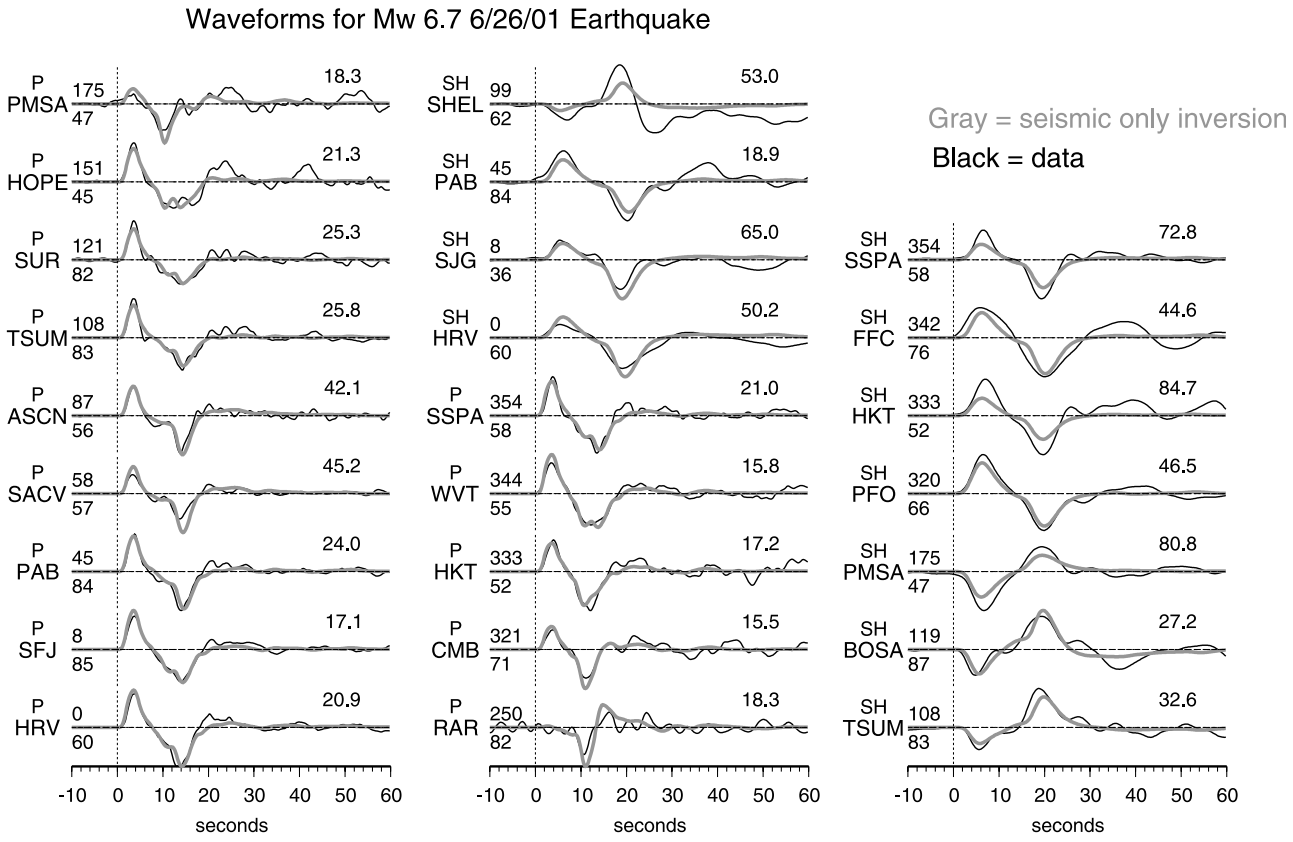

Figure 9. Teleseismic displacement data (P and SH) used in the slip inversion for the June 2001 aftershock (black lines) and calculated synthetics from the teleseismic-only inversion (gray lines). Conventions are the same as in Figure 4.

tion removed (the aftershock slip model is shown in Figure 17). Not surprisingly, the main difference is that when we remove the July aftershock, there is less slip in this location in the main shock model, although the overall seismic moment actually increases 5%, indicating the minimum intrinsic variation in moment estimates. Because of the uncertainty in the coseismic rupture model for the July aftershock, it is unclear whether the slip in the joint 2001 model southeast of the Harvard CMT location is real (Figure 11c). In any case, most of the slip during the main shock appears to have been released at the Harvard CMT location and to the northwest (Figure 11). In the remainder of this section, we remove our estimate of the deformation of the July aftershock from the geodetic data used in the inversions.

3.2.2. Fault Geometry

[30] We test different configurations of the fault plane, including fault planes with no change in dip (fixed to the Harvard CMT value of 18°), and two fault planes with a variety of dips (10–15° for the upper plane and 20–30° for the lower plane). We did a grid search over an even larger range of fault dips with just the geodetic data in a half-space to find the fault geometries with the lowest RMS misfits to the GPS and InSAR data. The range of lowest misfits was rather broad, but we select a fault plane near the middle of the minimum (Figure 18). The different fault geometries predict different seismic moments and maximum inferred slip.

[31] We allow inversions to explore a range of rupture velocities between 2.2 and 3.8 km/s and found an average value of 2.7 km/s. *Robinson et al.* [2006] found an average rupture velocity of 3.5 km/s for this event (the shear wave velocity in their crustal model), although the feature they call a "barrier" ruptures with an average velocity of 2.8 km/s.

3.2.3. Seismic Moment and Maximum Slip

[32] The seismic moment and maximum magnitude of slip depend on the data set(s) used, the fault geometry (particularly the dip), the elastic model, the number and size of subfaults and the type and extent of smoothing. The magnitude of slip and seismic moment are usually less in the InSAR-only inversions than in the GPS-only inversions. For example, given the fault geometry in Figure 18, the favored GPS seismic moment is 8.3×10^{21} N m (M_w 8.5) while the InSAR seismic moment is 4.0×10^{21} N m (M_w 8.3). The joint InSAR/GPS inversion has a moment of about 7.0×10^{21} N m (M_w 8.5). However, the misfit is only slightly greater (5% or so) if we choose a seismic moment for both data sets between 6 and 7×10^{21} N m (M_w 8.5). As with the 1996 earthquake, one explanation for the range in seismic moments is that any slip near the trench is poorly resolved by the geodetic data. Therefore, to alleviate this effect, we minimize the difference between the estimated moment and a value between the GPS and InSAR individual moment estimates: 6.2×10^{21} N m (M_w 8.5), although the data allow moments that are about 20% bigger or smaller than this value. Previous moment estimates based

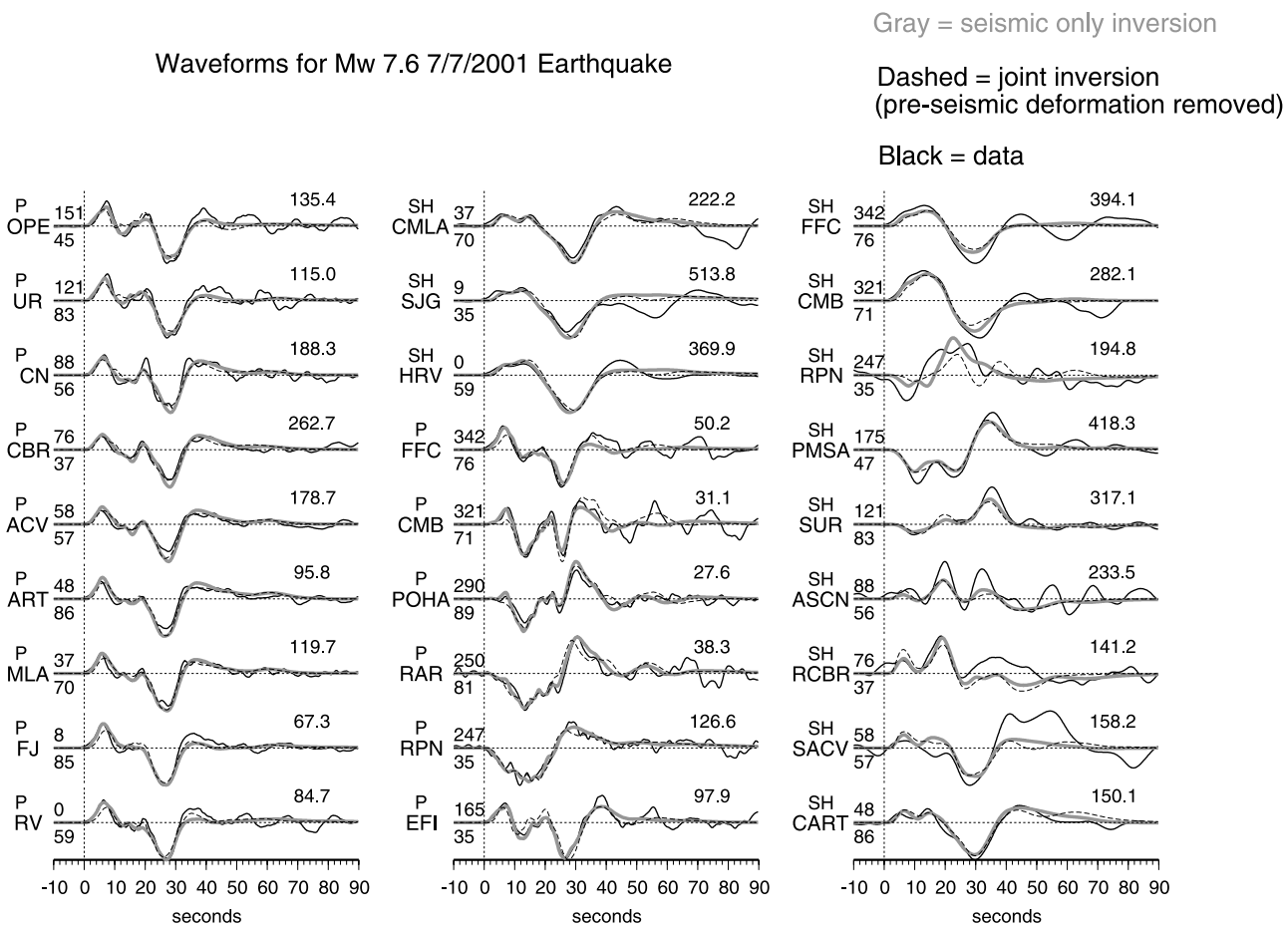

Figure 10. Teleseismic displacement data (P and SH) used in the slip inversion for the July 2001 aftershock (black lines) and calculated synthetics from the teleseismic-only inversion (gray lines), and from the joint inversion using the horizontal displacements from the Arequipa GPS station with the preseismic deformation removed, see text (dashed black lines). Conventions are the same as in Figure 4.

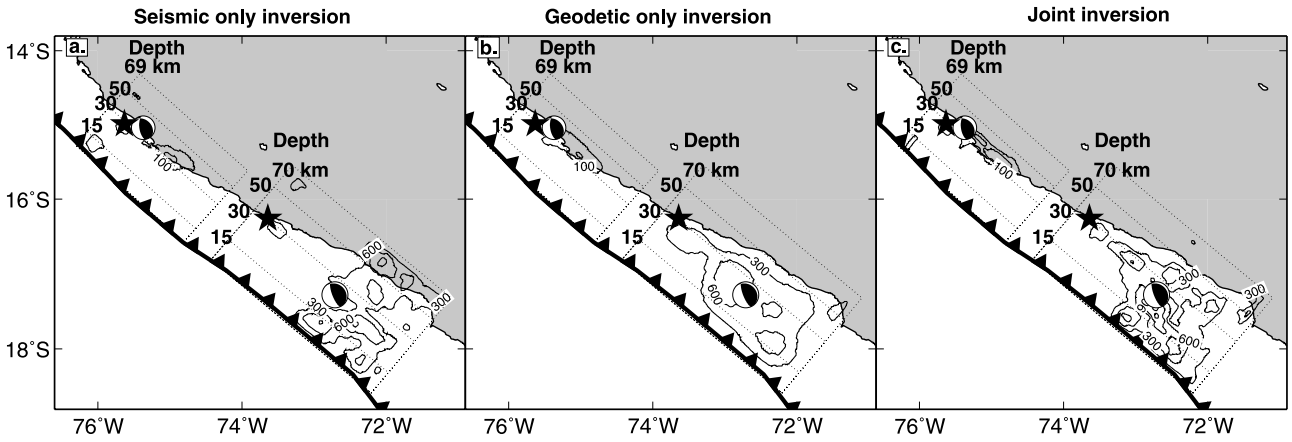

Figure 11. Contours of slip from the 1996 and 2001 earthquakes from inversions using (a) only seismic data, (b) only geodetic data, and (c) both data sets. For the 1996 earthquake, the maximum slip is about 3 m in the joint model and the contour interval is 1 m, while for the 2001 earthquake, the maximum slip is about 13 m (joint model), and the contour interval is 3 m. The NEIC location is shown as the black star, and the focal mechanism is from the Harvard catalog. Black barbed line indicates the trench location.

Table 3. Results of Our Model Inversions

Event	Moment, N m [M_w]			R[a]	T,[b] s	V,[c] km/s	S,[d]	M[e]	X[f]	Y[g]	Δ,[h] km	D[i]	H,[j] km
	Teleseismic	Geodetic	Joint										
1996	4.8×10^{20} [7.7]	4.6×10^{19} [7.7]	4.8×10^{19} [7.7]	50°	10	2.9	0.07	0.1	17	22	10	15°–30°	28
2001	6.2×10^{21} [8.5]	6.2×10^{21} [8.5]	6.3×10^{21} [8.5]	69°	14	2.7	0.1	0.1	22	35	10	11°–25°	30
26 Jun 2001	1.3×10^{19} [6.7]	N/A[k]	N/A	68°	2.7	3.2	0	0.1	10	20	5	22°	27
7 Jul 2001	3.2×10^{20} [7.6]	N/A	N/A	62°	9.2	2.9	0	0.1	17	20	5	15°–30°	20

[a]Mean rake.
[b]Mean risetime.
[c]Mean rupture velocity.
[d]Weight of smoothing constraint; all mean values are for the joint inversion and calculated using weighted averages (weighted by the slip).
[e]Weight of moment minimization constraint.
[f]Number of subfaults downdip.
[g]Number of subfaults along strike.
[h]Subfault size, same in both dimensions.
[i]Fault dip (may change with depth).
[j]Hypocenter depth.
[k]N/A (not applicable); earthquakes with only teleseismic data do not have geodetic-only or joint inversions.

on teleseismic data are between 2.4 and 5.8×10^{21} N m (M_w 8.2–8.5) [*Giovanni et al.*, 2002; *Bilek and Ruff*, 2002; *Tavera and Antayhua*, 2002; *Robinson et al.*, 2006] and the Harvard CMT moment is near the middle of this range: 4.7×10^{21} N m (M_w 8.4). *Ruegg et al.* [2001] used the Arequipa GPS station to find a moment of 4.4×10^{21} N m (M_w 8.4).

[33] As with the 1996 earthquake, we find that the seismic moment is about 10% lower when only a single dip for the fault plane is used, and the moment from the Wollard crustal velocity model has a moment that is 10% higher than with the Husen model. The general rupture characteristics are similar for all of these velocity models, and the geodetic RMS data fits are generally within 10% (most are unchanged).

[34] On the basis of just the geodetic data, the maximum magnitude of slip can vary significantly from 7 to 15 m. As expected, models with steeper dips or less smoothing have maximum slips toward the higher end of this range than shallowly dipping or highly smoothed models. Also, models without moment minimization can place large amounts of slip near the trench that is not resolved by the geodetic data. Other effects being equal, models with smaller subfaults have lower maximum slip (by several meters) than models with larger subfaults. The teleseismic studies also have a large range of maximum slips: 4.5 m [*Kikuchi and Yamanaka*, 2001], 8.4 m [*Bilek and Ruff*, 2002], and 11 m [*Giovanni et al.*, 2002].

[35] For the three large megathrust earthquakes we have studied (1995 and 1998 earthquakes in Chile and the 1996 and 2001 earthquakes in Peru, Figure 17), the maximum magnitude of slip is usually higher in the joint inversion than in the individual seismic or geodetic inversions. For example, for the 1995 earthquake, a static-only solution in a half-space gives a maximum slip of about 4 m [*Pritchard et al.*, 2002], while a static-only model with a different parameterization of subfaults in a layered elastic model has maximum slip of about 6 m. The joint teleseismic/geodetic inversion has maximum slip of 6.6 m. For the 2001 earthquake, the maximum slip from the different data sets are as follows: 12.8 m GPS; 9.6 m seismic; 7.4 m InSAR; 9.9 m GPS/InSAR; 12.8 m joint.

3.2.4. Comparing InSAR and GPS data

[36] We directly compare GPS and InSAR where they overlap (Figure 19), and where all three components of GPS deformation exist (which we project into the LOS). This comparison requires a correction for the orbital errors for each InSAR track. Although the correction depends slightly on the fault geometry used, in general the RMS misfit

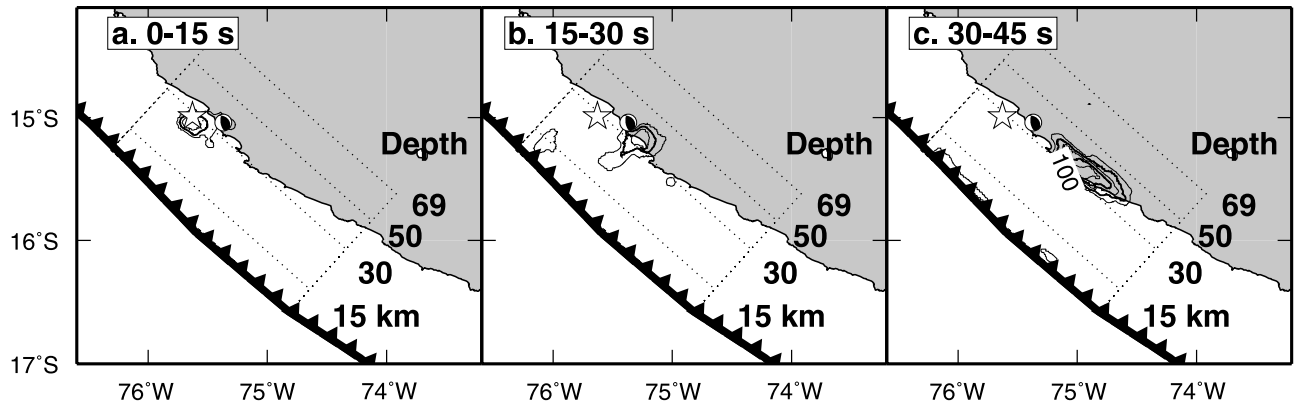

Figure 12. Spatiotemporal evolution of fault slip from the joint inversion of the 1996 earthquake during 5 s windows with 0.5 m contours. The hypocenter from the NEIC is shown as a white star, the trench is the black barbed line, and the mechanism is from the Harvard CMT catalog. Fault slip after 45 s is small.

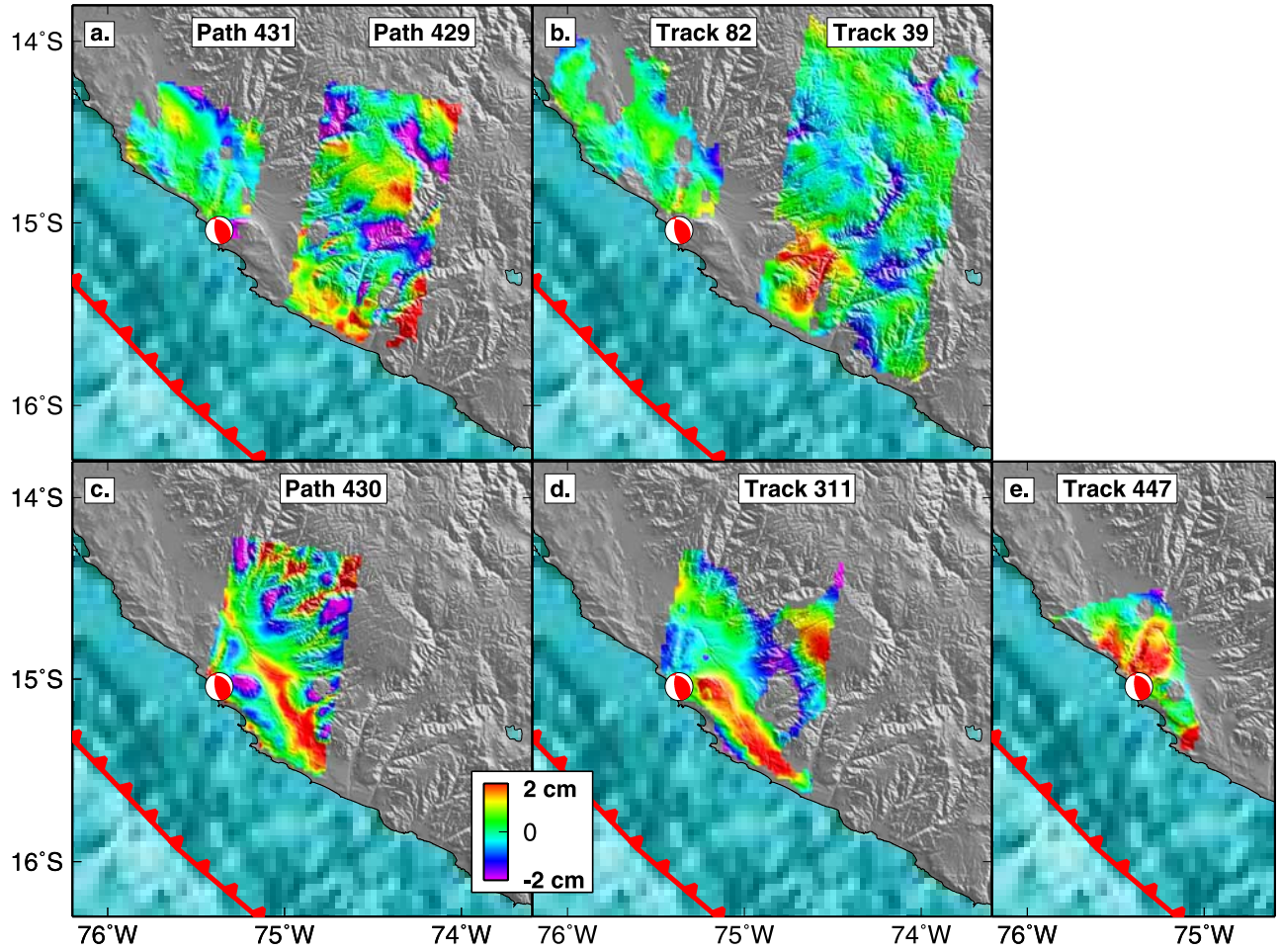

Figure 13. InSAR residuals from our best fit model for the 1996 earthquake (data from Figure 2, joint model from Figure 11) plotted over shaded topography and bathymetry with the trench shown as a red barbed line. RMS misfits between data and the three models are in parenthesis (teleseismic-only; geodetic-only; joint). Because orbital ramps for the InSAR are not calculated during the teleseismic-only inversions, to make the comparison similar, we solve for the ramp parameters that minimize the misfit. (a) JERS paths 429 (2.6 cm; 1.5 cm; 1.6 cm) and 431 (1.1 cm; 1.0 cm; 0.9 cm). (b) ERS tracks 82 (1.1 cm; 0.4 cm; 0.6 cm) and 39 (2.0 cm; 0.7 cm; 0.7 cm). (c) JERS path 430 (2.8 cm; 1.3 cm; 1.3 cm). (d) ERS track 311 (2.5 cm; 1.1 cm; 1.1 cm). (e) ERS ascending track 447, (1.9 cm; 1.2 cm; 1.3 cm).

between the GPS and InSAR is about 2 cm, and is smaller than the RMS found in other areas [e.g., *Pritchard et al.*, 2002]. However, the mean offset is surprisingly large at 3 cm. The mean offset is in part due to the station with the largest offset (JHAI), which seems to favor slip in different locations than the InSAR data (see discussion below). The overall value of the RMS is expected, given the intrinsic errors in the vertical GPS which dominates in the comparison with InSAR (about 1 cm, see Table 2) and the InSAR data accuracy is probably also of order 1 cm in southern Peru (based on the misfit between the data and slip models Figures 13 and 14). The misfit between the GPS data and the slip models is usually greater than 3 cm, particularly in the east component (Figure 5), which is larger than the formal errors of 0.5 cm or less (Table 2).

3.2.5. Comparing Seismic and Geodetic Inversions

[37] Because we use only two strong motion stations, we have not done a strong motion only inversion, but there is little difference between a slip model using just the teleseismic data or one using the teleseismic and strong motion data (Figure 8). However, in order to fit both the teleseismic and strong motion data, we have to expand the range of allowed rupture velocities from 2–3 to 2–4 km/s.

[38] The teleseismic-only and geodetic-only models of slip have several differences. As previous workers have noted, most slip in the teleseismic-only model is located about 120 km southeast of the hypocenter (the main asperity), with a few other regions of enhanced slip [*Kikuchi and Yamanaka*, 2001; *Giovanni et al.*, 2002; *Bilek and Ruff*, 2002]. There are also two pulses in the GPS inversion [*Norabuena*, 2004], but based on our resolution tests, the slip distribution in this area is almost completely controlled by a single station (JHAI). On the other hand, slip in the InSAR-only model is more continuous between the hypocenter and the main asperity. In addition, slip in the geodetic-only models is mostly located about 20 km deep, while there are two peaks in the teleseismic slip at about 60 km and 15 km depth. We comment on possible

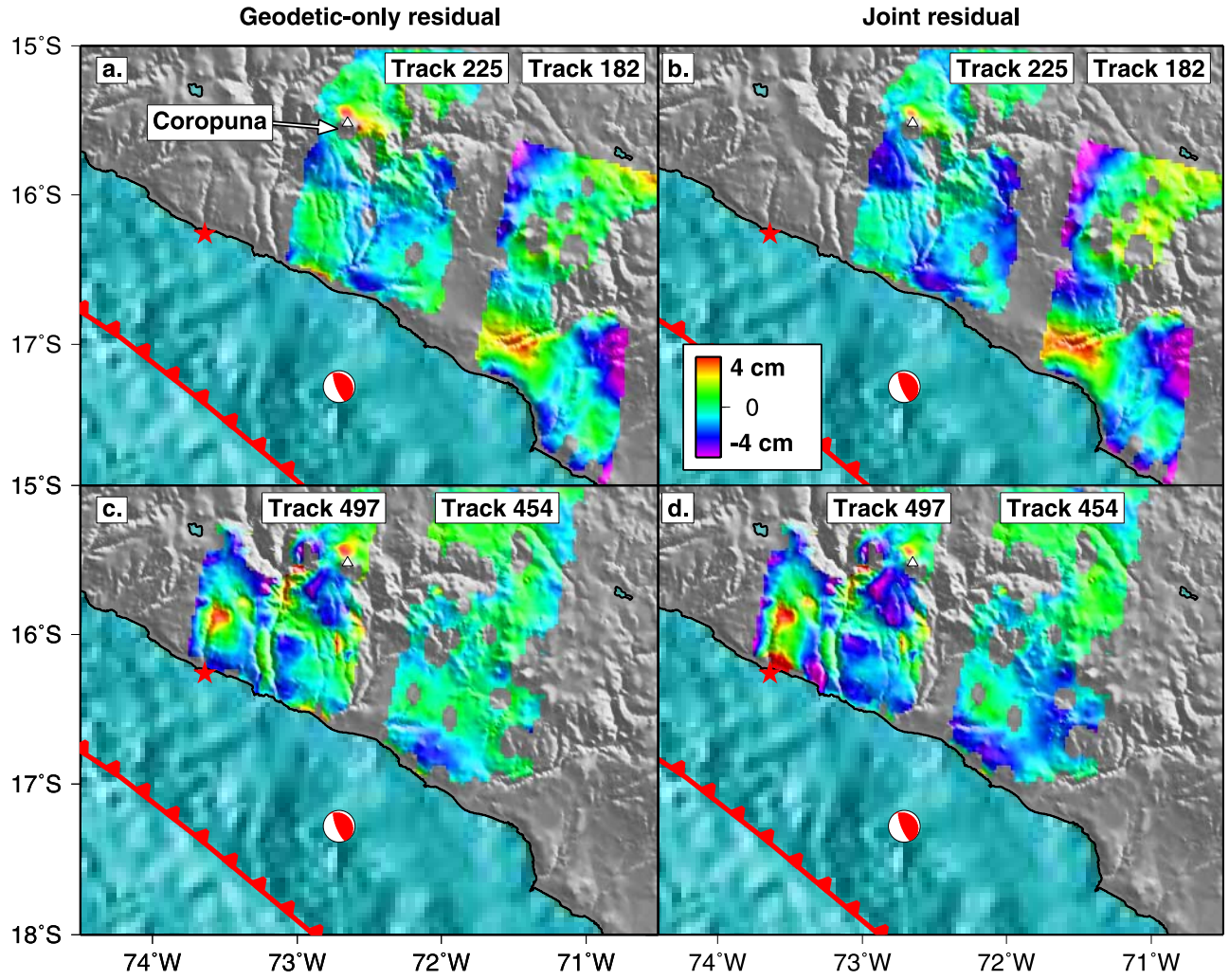

Figure 14. InSAR residuals from our best fit models for the 2001 earthquake (data from Figure 6) plotted over shaded topography and bathymetry with the trench shown as a red barbed line. Residuals from the geodetic-only model are shown for (a) ERS tracks 225 and 182 and (c) ERS tracks 454 and 497, while residuals from the joint model are (b) and (d). RMS misfits between data and the three models are in parentheses (teleseismic-only; geodetic-only; joint). Track 454: (11.0 cm; 0.8 cm; 1.0 cm); track 225: (9.9 cm; 1.1 cm; 1.0 cm); track 182: (8.9 cm; 1.7 cm; 2.2 cm); track 497 (10.1 cm; 1.6 cm; 2.0 cm); track 404 (5.1 cm; 1.5 cm; 1.8 cm); track 89 (7.3 cm; 1.2 cm; 1.5 cm); and RADARSAT: (10.8 cm; 1.2 cm; 1.7 cm). Several tracks of data show residuals north of Coropuna volcano (white triangle), see text.

explanations for the differences between the geodetic-only and teleseismic-only models in the discussion.

[39] While slip in the joint model is concentrated on an asperity about 120 km from the hypocenter, there is also more slip between the hypocenter and Harvard CMT location than in the teleseismic-only model. Slip is also shallower in the joint model than in the teleseismic-only model, mostly confined to less than 50 km. In spite of these differences between the models, the fit to the teleseismic waveforms is nearly the same for both models (Figure 7). While the RMS misfit to the geodetic data increases by adding additional data sets, the geodetic-only and joint models reduce the variance by 75–95% (Figure 14).

3.2.6. Features in the Residual Interferograms

[40] In several InSAR tracks (497, 225, and 454), we observe a consistent residual of a few centimeters of primarily subsidence north of Coropuna volcano (Figure 14). Although the exact timing is poorly resolved, we think that the deformation is shallow (less than a few kilometers) and we hypothesize that it may be related to groundwater flow that was enhanced by coseismic shaking [*Pritchard*, 2003]. Postseismic pore pressure increase has been proposed elsewhere to explain the increased streamflow following several earthquakes [*Manga et al.*, 2003], and is plausible considering previously established distance-magnitude relations for the proposed phenomena [*Manga*, 2001]. We cannot rule out shallow earthquakes as a cause of the deformation, but there are no events with the corrected depth and location to explain the deformation [*Pritchard*, 2003].

3.2.7. Misfit to the GPS Data

[41] The largest misfit to the GPS data is at station TANA (Figure 20), and is about 10–20 cm in the east component. This station moves almost due west, which is anomalous

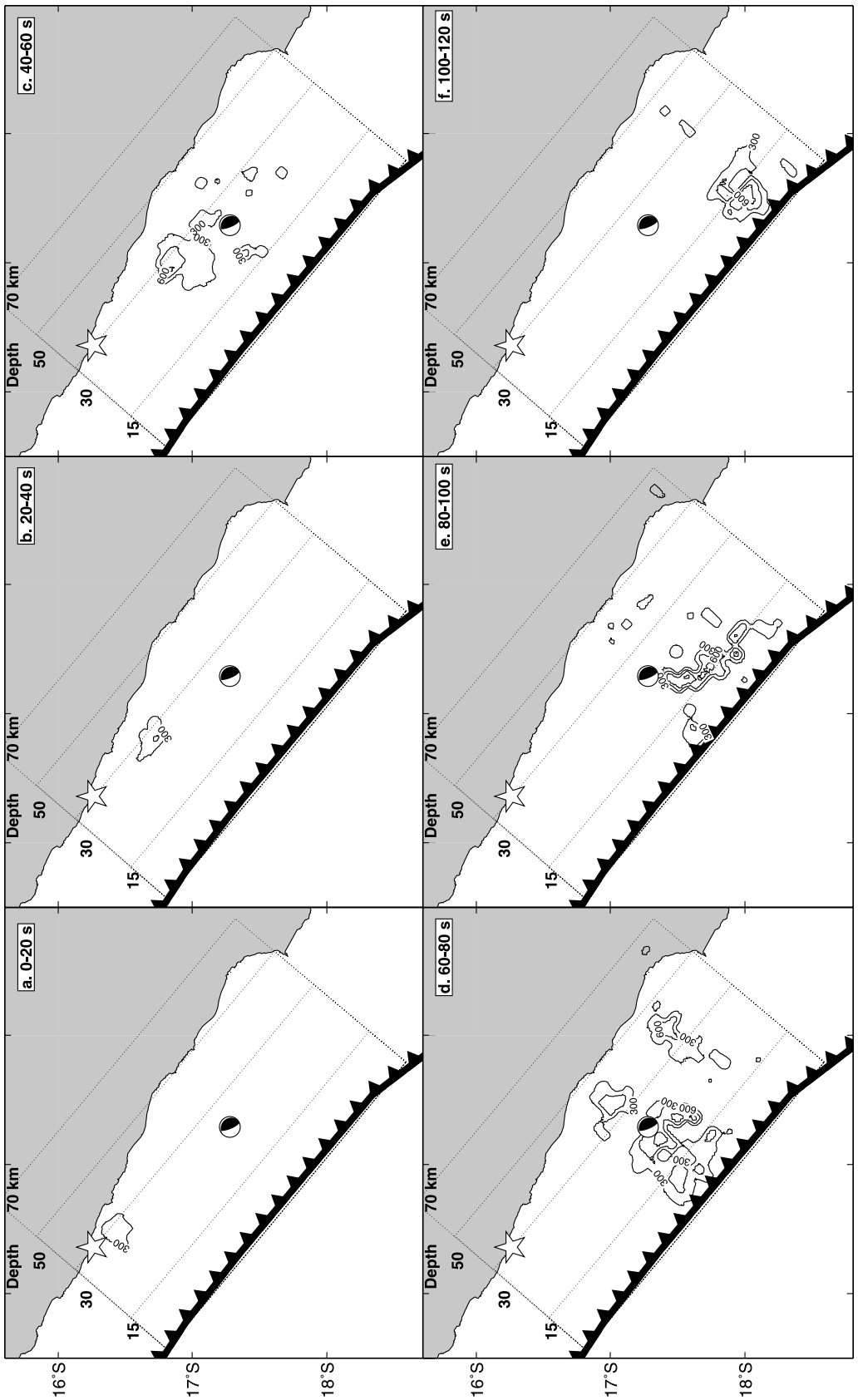

Figure 15. Spatiotemporal evolution of fault slip from the joint inversion of the 2001 earthquake during 20 s windows with 3 m slip contours. The hypocenter from the NEIC is shown as a white star, the trench as a black barbed line, and the mechanism is from the Harvard CMT catalog. Fault slip after 120 s is relatively small.

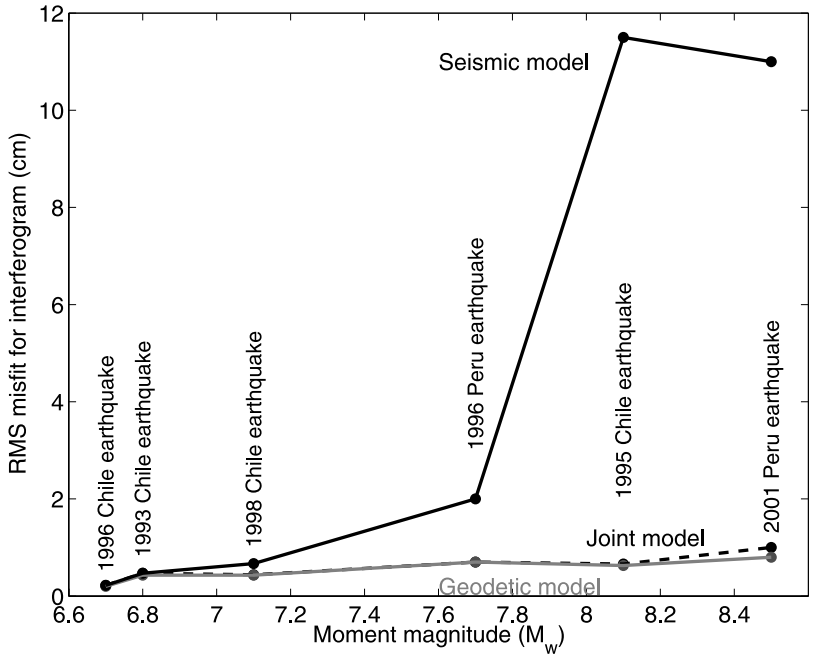

Figure 16. RMS misfit to selected interferograms spanning six subduction zone earthquakes from different slip models using different combinations of data, seismic-only (black line), geodetic-only (gray line), and joint (dashed black line). The earthquakes and interferograms used to make this figure were from southern Peru (1996 and 2001 earthquakes, tracks 39 and 454, respectively) and northern Chile (1995 M_w 8.1, 1996 M_w 6.7, 1998 M_w 7.1, all track 96; 1993 M_w 6.7, track 325) [*Pritchard et al.*, 2006].

compared to the southwest motion of the other stations (Figure 5). To reduce the residual, the fault plane must be extended north of the hypocenter to near the TANA station [*Norabuena*, 2004] (Figure 17) with slip equivalent to about a M_w 7.1, that occurred between the occupation dates of this station (16 July 1999 and 28 June 2001). The deformation may be postseismic from the 1996 earthquake, anomalously large interseismic deformation, or associated with the 2001 earthquake (preseismic, coseismic, or postseismic). Three interferograms that we have that span this time interval do not reveal deformation near the TANA station: data from track 404 have a master scene on 29 December 1998 and slave scenes 31 July 2001 and 16 July 2002 and data from track 39 spans 3 January 1997 and 23 December 1999 [*Pritchard*, 2003]. For now, we assume that there was some significant slip north of the hypocenter, but since the timing of slip is not known and its spatial extent is not well resolved, we do not include this slip in our plots of coseismic slip, but do include it in Figure 17.

3.3. The 2001 Aftershocks

[42] Slip from the June and July 2001 aftershocks is shown in Figure 17, and the predicted waveforms are shown in Figures 9 and 10. Mean properties of the rupture (risetime, rupture velocity, moment, rake) are in Table 3.

[43] For the June aftershock, our preferred model (see Figure 18) has a depth of 27 km (the same as the National Earthquake Information Center (NEIC) depth), although the fit is about the same at the Harvard CMT depth (24 km). Considering that these inferred parameters are derived using different crustal seismic velocity models, exact agreement is not expected. The final slip distribution is a simple point source (Figure 17), and appears to be about 40 km away from the CMT location. As in northern Chile, it seems that the Harvard CMT locations are shifted trenchward for events smaller than about M_w 7.5 [*Pritchard et al.*, 2006].

[44] Displacement from the June aftershock at the Arequipa GPS station is not clearly above the noise threshold, but is consistent with the predicted values: N: -0.5 to 0 cm observed, -0.6 cm predicted; E: -1 to -0.5 cm observed, -0.8 cm predicted; V: 0 ± 1 cm observed, 0.8 cm predicted (using data from SOPAC http://sopac.ucsd.edu/ and *Melbourne and Webb* [2002]).

[45] Our model of the July aftershock predicts displacements that are close to the total observed offsets (predicted N = -3.1 cm; E = -2.7 cm; V = -0.2 cm; and observed N = -3.0 ± 0.6 cm; E = -2.5 ± 0.4 cm; and effectively zero for the vertical [*Melbourne and Webb*, 2002]). However, *Melbourne and Webb* [2002] attribute -2 ± 0.5 cm of north motion and -1 ± 0.5 cm of east motion to preseismic deformation. If the preseismic motion is real, our teleseismic prediction of surface deformation is too large.

[46] If we force our solution to match the preseismic corrected displacements, the slip distribution changes significantly. In particular, the rupture becomes more bilateral, but the fit to the waveforms is not as good (Figure 10) and does not improve if we change the fault dip and hypocenter depth. In our original inversion, the rupture is predominately to the northwest, consistent with the relative locations of the hypocenter and Harvard CMT locations. Some rupture to the southeast is apparent in our original model, but this model is not as bilateral as suggested by previous

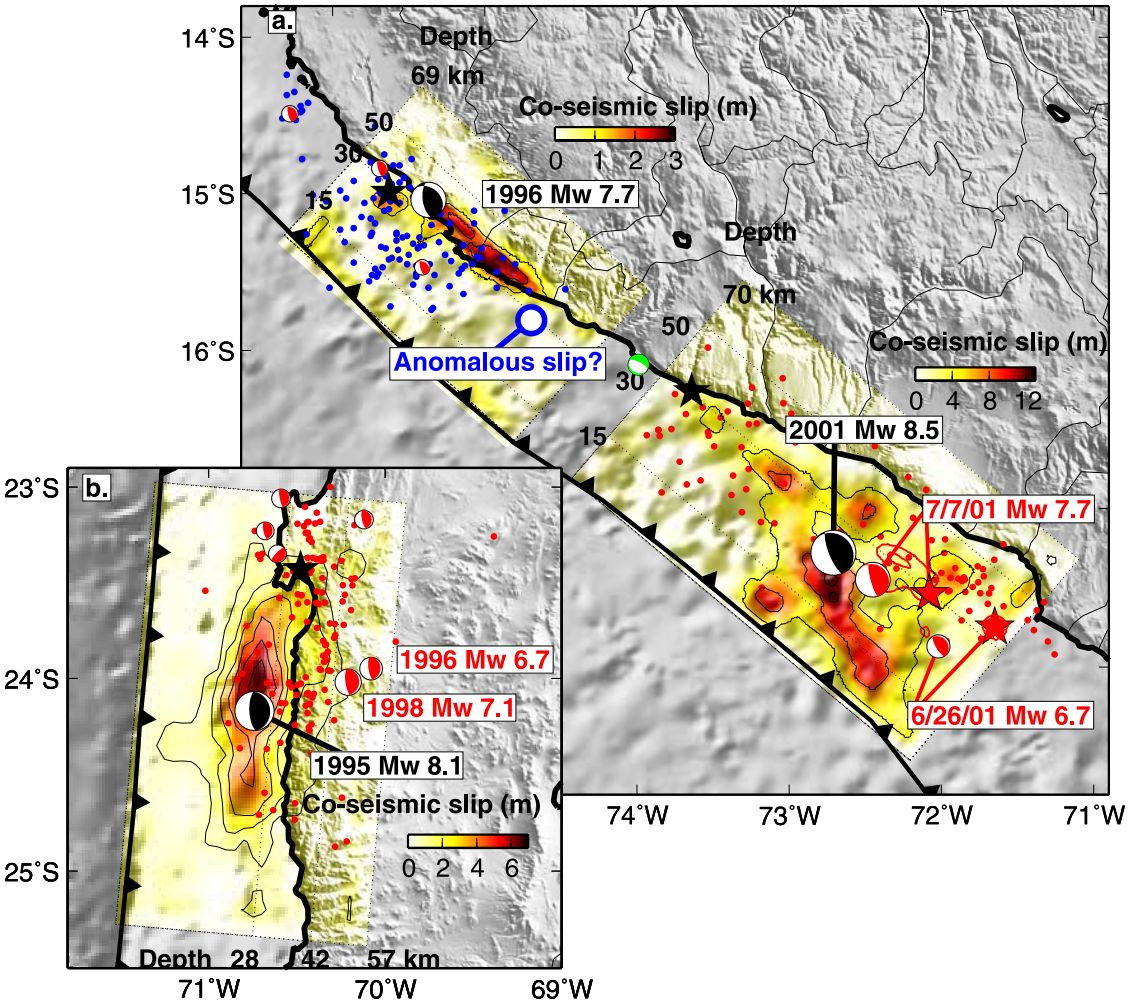

Figure 17. Contours of slip from the 1996 and 2001 Peru and 1995 Chile earthquakes plotted over shaded topography and bathymetry. In all maps, the black stars are the NEIC hypocenter locations for the main shocks, black CMT mechanisms are for the main shocks, circles are aftershock locations, black dotted lines show depth intervals on the slab, black barbed lines are the trench, and red mechanisms are CMTs with $M_w > 6$. Aftershock with green mechanism is probably not located on the fault interface. (a) The 2001 earthquake is shown with slip contours every 4 m with relocated small aftershocks as red dots [*Giovanni et al.*, 2002]. Slip contours from the June and July aftershocks are shown in red (1 m contour for July and 40 cm for June). Red stars indicate the NEIC hypocenters. Slip from the 1996 earthquake is shown with 1 m contours. Aftershocks shown as blue dots are from the NEIC catalog between 12 November 1996 to 12 May 1997. The blue hollow circle labeled anomalous slip is the approximate location of fault slip needed to explain the displacement at the station TANA (see text). (b) Slip from the 1995 Antofagasta, Chile, earthquake shown with 1 m contours (from the joint teleseismic and geodetic inversion [*Pritchard et al.*, 2006]). Aftershocks shown as red dots have $M_w > 2.5$ and were located by a local network [*Husen et al.*, 1999]. Harvard CMT mechanisms for the 1996 and 1998 earthquakes have been shifted to the east to the NEIC location [see *Pritchard et al.*, 2006].

teleseismic studies [*Bilek and Ruff*, 2002; *Giovanni et al.*, 2002].

4. Discussion

4.1. Comparing Seismic and Static Inversions

[47] For both the 2001 and 1996 earthquakes, there are differences between the seismic-only and geodetic-only inversions. Slip in the seismic-only models is localized in one or two regions (also known as asperities). The geodetic-only models usually have enhanced slip in the same regions as the seismic-only models, but in addition, have a smoother slip distribution, such that slip appears more continuous between the hypocenter and the southern extent of rupture. The difference between seismic-only and geodetic-only models is more obvious for the 2001 earthquake, but perhaps this is simply a result of the larger rupture spreading out the slip more. By comparison, the 1995 M_w 8.1 Antofagasta earthquake has regions of enhanced moment release, yet the teleseismic-only models of slip are more continuous than the 1996 and 2001 slip distributions [*Pritchard et al.*, 2006]. In any case, the seismic and

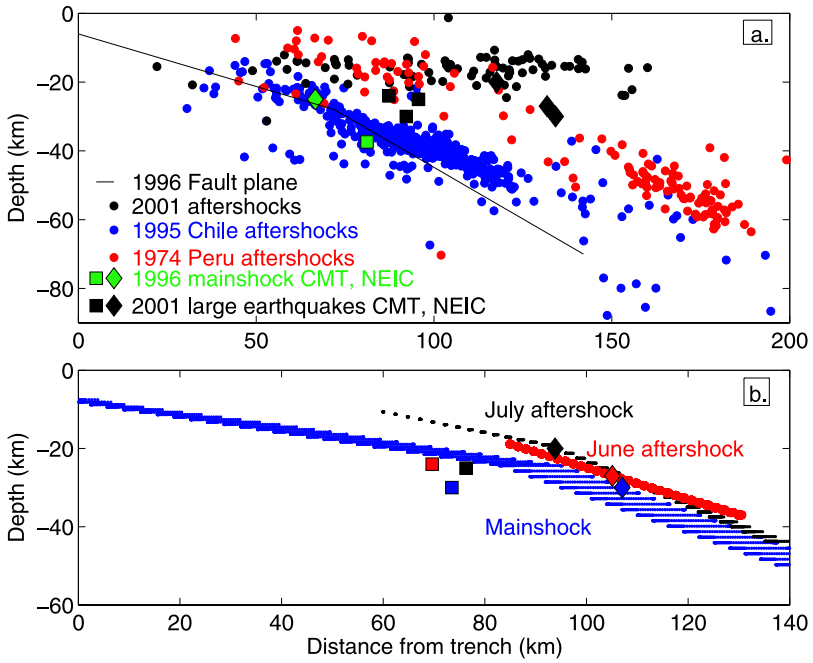

Figure 18. (a) Earthquake and aftershock locations from subduction zone earthquakes in northern Chile and southern Peru, showing a range in inferred fault geometries. Relocated aftershocks of the 2001 main shock (black circles) [*Giovanni et al.*, 2002] do not locate the fault interface well. For the 2001 main shock and the June and July largest aftershocks, the CMT (black squares) and NEIC hypocenters (black diamonds) indicate a fault plane that has a dip more similar to the inferred fault plane that ruptured in the 1974 Peru earthquake (red circles) [*Langer and Spence*, 1995], than the inferred subduction interface in northern Chile (inferred from the aftershocks of the 1995 earthquake, blue circles) [*Husen et al.*, 1999]. On the other hand, the 1996 Peru earthquake has a CMT location (green square), NEIC hypocenter (green diamond), and inferred fault plane used in our modeling (black line) [e.g., *Spence et al.*, 1999] similar to the rupture plane of the 1995 earthquake. (b) Inferred fault planes for the 2001 main shock as well as the June and July aftershocks. The CMT locations are shown as squares and the NEIC hypocenters are represented as diamonds. The dip and depth of the fault planes for the June and July events were constrained by the NEIC hypocenters and fits to the teleseismic waveforms. The 2001 main shock fault plane (blue circles) is constrained by the NEIC hypocenter, and a grid search of the best fitting fault geometry for the geodetic data (see text).

geodetic data are relatively consistent since the misfit to each data set from the joint models for the 1996 and 2001 earthquakes is only negligibly more than the misfit using either data set by itself (Figures 4, 7, 16, and 14).

[48] We do not think that the difference between the seismic-only and geodetic-only models is an artifact of the inversion methodology. Some have argued that geodetic-only inversions of earthquake slip are oversmoothed [e.g., *Wald et al.*, 1996], although this is not a universal result, and might depend on the inversion strategy [e.g., *Segall and Davis*, 1997]. While this explanation is plausible, we do not favor it because when we use the same methodology in northern Chile, the teleseismic-only model is similar in terms of the continuity of slip to the geodetic-only result.

[49] Further, we do not think that the difference is an artifact of postseismic (or interseismic) deformation contaminating the geodetic data. While the available geodetic data indicate significant postseismic deformation following the 2001 earthquake equivalent to 20–40% of the coseismic moment [e.g., *Ruegg et al.*, 2001; *Melbourne and Webb*, 2002; *Pritchard*, 2003], it is not sufficient to explain the meter-scale differences in the teleseismic-only and InSAR-only slip models. Also, while the primary discrepancy between slip in the InSAR model and the teleseismic model is located between the hypocenter and CMT locations, we find that although not well resolved, most of the after slip is in another location immediately downdip of the CMT location (E. O. Norabuena et al., manuscript in preparation, 2007).

[50] For the 1996 earthquake, it is impossible to separate postseismic deformation during the first 51 days from the coseismic deformation. Yet, there is no evidence for deformation between January 1997 and December 1999 [*Pritchard*, 2003]. Although we cannot rule out an after slip explanation of the discrepancy between the geodetic-only and seismic-only inversions for the 2001 earthquake, there is no compelling evidence for this explanation either.

[51] We propose that the difference between the teleseismic-only and geodetic-only models simply reflects the different inherent abilities of the seismic and geodetic data to resolve slip during large earthquakes. If slip occurs slowly in some parts of the rupture, it may not generate seismic waves. Slow slip was possibly a component of the 2004 great Sumatra-Andaman earthquake [*Lay et al.*, 2005], but occurred at a timescale of less than 10 minutes [*Hjorleifsdottir et al.*, 2005]. A slow rupture would be

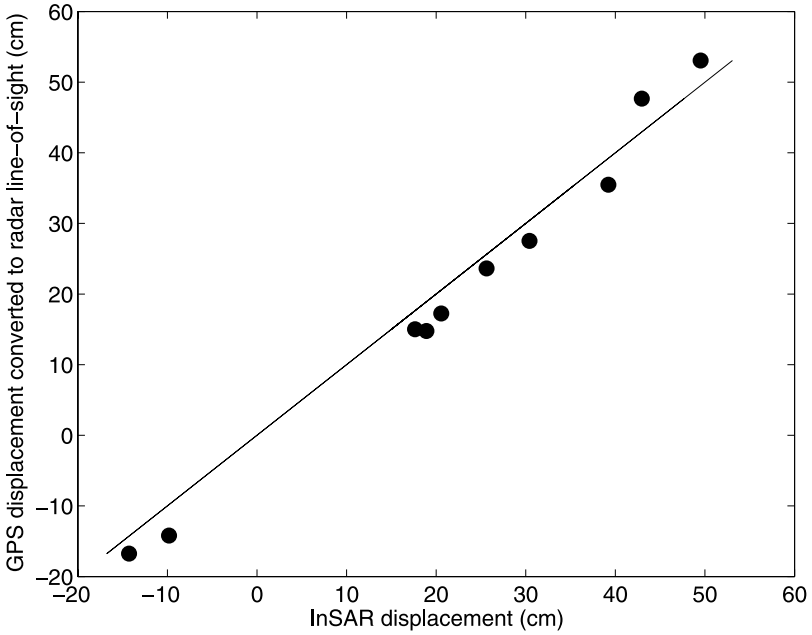

Figure 19. Comparison between 10 GPS displacements from the 2001 earthquake projected in the radar LOS (from four independent GPS stations) and InSAR observations from six satellite tracks. The independently determined best fit quadratic ramp (which accounts for orbital errors) from our preferred joint seismic and geodetic coseismic model has been removed from the InSAR data. Error bars on the GPS observations are smaller than the size of the plotted points. The RMS difference and mean offset are 1.7 cm and 3.1 cm, respectively.

characterized by a long risetime. While the risetime is not well resolved here, we do not observe any consistent spatial variations within the rupture areas. *Robinson et al.* [2006] infer that there is anomalously slow slip and a stalled rupture front in exactly this area (between the hypocenter and Harvard CMT location), but because of the nonuniqueness of the teleseismic-only inversions for two-dimensional fault slip from $M_w > 7.5$ earthquakes [e.g., *Pritchard et al.*, 2006] these features are not required by the data. We suggest that for the 2001 earthquake, the geodetic data resolves slip between the hypocenter and Harvard CMT location that is not well resolved by the seismic data between the large seismic asperities at the hypocenter and about 100 km to the southeast. Conversely, the largest seismic asperity appears to be located offshore near the trench, an area that is poorly resolved by the geodetic data. The anomalously slow slip between the hypocenter and Harvard CMT location is coincident with the location of a subducting ridge and trough on the Nazca Plate, suggesting a possible causal relationship [*Robinson et al.*, 2006].

[52] There is a difference between the GPS and InSAR coseismic slip distributions for the 2001 earthquake: the InSAR model shows continuous slip between the hypocenter and CMT location, while the GPS model has two pulses of slip more similar to the seismic results. As already noted, the GPS slip distribution in this area is largely controlled by a single station, while several tracks of InSAR constrain the slip distribution here.

4.2. Distribution of Slip

[53] We compare the slip distributions for the 1995, 1996, and 2001 earthquakes in Figure 17. For all three events, the maximum slip during the rupture occurs 50–100 km from the hypocenter, as observed in other earthquakes, like the 1974 southern Peru event [e.g., *Giovanni et al.*, 2002]. Using the 0.5 m slip contour for reference, we find a maximum depth of rupture during the 1995 earthquake to be about 45 km [*Pritchard et al.*, 2006], while the 1996 and 2001 earthquakes ruptured to about 50 km (although the 2001 earthquake had some deeper slip). Our depth for the 1996 earthquake is shallower than some teleseismically derived slip distributions (66 km [*Spence et al.*, 1999]) but is similar to the only previous result that included geodetic data [*Salichon et al.*, 2003]. The 1996 earthquake has a greater portion of its moment release beneath land than the other two events, and this might be related to subduction of the Nazca ridge.

[54] There is a clear gap between the areas that ruptured in the 1996 and 2001 earthquakes (Figure 17), which could accommodate a $M_w > 7.5$ earthquake. This region may have last ruptured in 1913 [e.g., *Kelleher*, 1972].

[55] Significant slip in the teleseismic-only models for the 1995 and 2001 earthquakes occurs at the downdip limit of the model parameterization, while this is not true for the 1996 earthquake. We interpret the existence of slip at the edges of the model parameterization to mean that slip is poorly resolved by the teleseismic data in the rupture of these large events. However, the source time function of the 1995 and 2001 ruptures (also known as line sources of slip) are more consistent between inversions with the different data sets.

4.3. Aftershocks

[56] The distribution of large aftershocks ($M_w > 6$) is different for the 1995 northern Chile earthquake and the

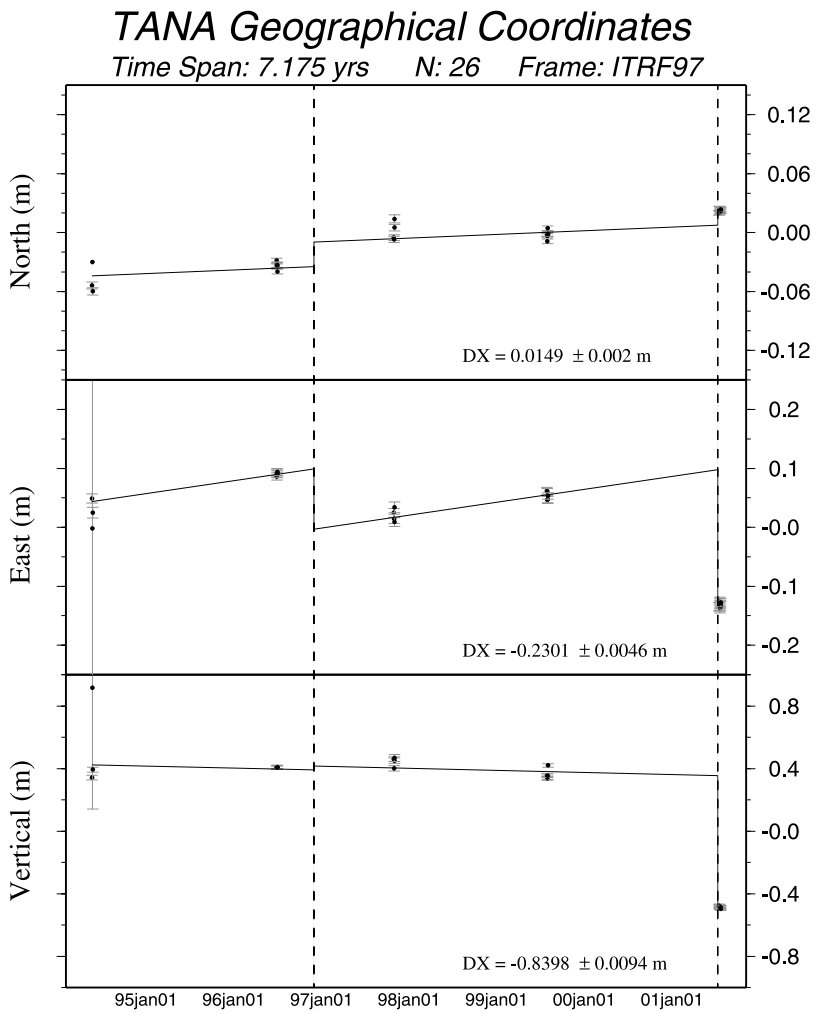

Figure 20. Position of GPS station TANA is shown in three dimensions before and after the 1996 and 2001 earthquakes (shown by the vertical lines). The daily solutions are shown by the black circles with one standard deviation error bounds. The inferred 2001 coseismic offset and error is listed for each component as DX (see also Table 2), although the vertical component was not used in the modeling (see text).

1996 and 2001 southern Peru earthquakes (Figure 17). For 1995, the largest aftershocks occur downdip of the coseismic rupture up to 2.5 years after the event [*Pritchard et al.*, 2006]. Following the 1996 and 2001 earthquakes, the largest aftershocks were either at the same depth or shallower than the region that ruptured in the main shock, and occurred within a few weeks of the main shock. The majority of moment release in the July 2001 aftershock appears near the main asperity of the 2001 main shock, and although not well resolved, the areas that slipped in the main shock and largest aftershock do events do not appear to significantly overlap.

4.4. Directivity

[57] There is a pattern of earthquake directivity along the coast of western South America (Figure 1). In the north, earthquakes rupture to the north (1979 M_w 8.2 Colombia event [*Kanamori and Given*, 1981; *Beck and Ruff*, 1984]), in the middle, earthquakes are bilateral (1996 M_w 7.5 Peru earthquake [e.g., *Ihmlé et al.*, 1998], the 1960 M_w 7.6 Peru earthquake [*Pelayo and Wiens*, 1990], and the 1966 M_w 8.0 Peru event [*Beck and Ruff*, 1989]), and south of about 12°S, directivity is southerly (the 1960 M_w 9.5 Chile event [e.g., *Benioff et al.*, 1961]; the 1974 M_w 8.1 Peru event (bilateral, but most moment to south [*Langer and Spence*, 1995]); and the 1985 M_w 8.0 Chile event (ruptured updip and to the south [*Choy and Dewey*, 1988; *Mendoza et al.*, 1994]), as well as the 1995, 1996, and 2001 earthquakes). On the basis of these patterns, we hypothesize that the future rerupture of the 1877 earthquake will rupture to the south.

[58] The factors that control earthquake directivity are poorly understood. In a global study, *McGuire et al.* [2002] find that most earthquakes are unilateral, and fault segmentation might explain this observation for large earthquakes. However, no explanation is given for ruptures favoring one direction over the other (i.e., the preference for ruptures to the south in southern South America). Possible explanations include: the history of previous earthquake ruptures, preferential orientation of structures on the fault interface due to oblique convergence, or the superposition of different

materials across the fault zone [e.g., *Rubin and Gillard*, 2000].

5. Conclusions

[59] We have used all available data (teleseismic, geodetic and strong motion) to determine the distribution of slip during four earthquakes M_w 6.7–8.5 in southern Peru. For all events, the seismic moment depends on the data used and model parameterization (velocity model, dip, etc.). Thus discrepancies in moment estimated by different authors using different methods and data do not necessarily reflect any underlying processes occurring on the fault plane, but the fundamental nonuniqueness of inferred models from available data. The detailed slip distributions from the teleseismic-only and geodetic-only data are slightly different for the 1996 earthquake and significantly different for the 2001 earthquake. The first 45 s or so of the 2001 earthquake rupture appear similar to the 1996 rupture, but subsequently, a much larger amount of slip occurred producing the larger magnitude. The depth of maximum coseismic rupture and the distribution of large aftershocks ($M_w > 6$) is different between the 1995 and 2001 earthquakes, and may partly explain the variations in the amount of after slip following these events, but other explanations are also possible [*Pritchard*, 2003].

Appendix A: Modeling Strategy

[60] We use the technique of *Ji et al.* [2002] to invert for fault slip for all earthquakes using both the seismic waveforms and geodetic data. The seismic waveforms are transformed into the wavelet domain so that both the temporal content (which contains information about the spatial location of slip) and frequency content (which constrains the duration of rupture on each patch, also called the risetime) of the waveforms are used. Further information, including tests of the resolving power are given in *Ji et al.* [2002], and a discussion of the application of this method to dip-slip faults with InSAR and GPS is given by *Pritchard et al.* [2006].

[61] We compute the synthetic waveforms and static displacements in both layered and half-spaces. We are not aware of a detailed crustal velocity model for our specific study area, so we try models from regions to the north [*Wollard*, 1975; *Hartzell and Langer*, 1993] (henceforth called the Wollard model), and south [*Husen et al.*, 1999] (called the Husen model). We convert the velocities to density following *Ludwig et al.* [1970], which has been successfully used to model gravity in northern Chile in regions with little partial melt [*Schmitz et al.*, 1997]. We use the same P and S quality factors (Q) for all layers (1500 for P, 600 for S). We convolve the attenuation function [t^*, e.g., *Lay and Wallace*, 1995] with the synthetics to account for attenuation of the teleseismic waveforms using typical values (1 second for P and 4 seconds for S). When calculating the InSAR displacements, we account for the variations in the incidence angle across the radar scene.

[62] The dip of the interface between the South American and Nazca plates is about 25–30° [*Hasegawa and Sacks*, 1981; *Grange et al.*, 1984], but the detailed shape of the interface, particularly the variations of dip as a function of depth, are not well known [*Spence et al.*, 1999] (Figure 18), and these details can impact slip inversions [e.g., *Hartzell and Langer*, 1993]. On the basis of relocated aftershocks from the 1996 earthquake, a hinge in the plate at 25 km is suggested, where the slab dip changes from 10–12° to 25–55° [*Spence et al.*, 1999] (Figure 18). A hinge in about the same location was also seen in the aftershock sequence following the nearby 1974 M_w 8.1 Peru event [*Langer and Spence*, 1995] (Figure 18). We test a variety of different slab geometries for all earthquakes. We constrain the updip location of the fault to be at the trench. Because the 1996 earthquake occurred near the location where the Nazca Ridge is subducting, there is some complexity in defining the trench location. The ridge is 1.5 km above the surrounding ocean floor [*Schweller et al.*, 1981], so there will be undulations of the fault interface, but the magnitude and location of these undulations are not constrained. On the basis of bathymetric data [*Schweller et al.*, 1981], we assume that the trench in the area of the 1996 earthquake is 6 km deep, and 7 km in the location of the 2001 earthquake. For all earthquakes we discretize the fault with uniform patches, but use different sizes depending on the size of the earthquake (Table 3).

[63] We use simulated annealing [*Rothman*, 1986] to find the best fit model parameters: the slip amplitude and direction, rise time, and rupture velocity, with extremal bounds on each parameter. For example, we constrain the rake of the 1996 earthquake to be between 20 and 90°, while for the 2001 the rake is between 40° and 120°. The risetime indicates the length of time it takes for the fault patch to slip (prescribed as a modified cosine function [*Hartzell et al.*, 1996]) and the rupture velocity specifies the speed of the local rupture front. In addition, we solve for quadratic ramps for the InSAR data as part of the inversion process. We define the best fit model as having the lowest objective function, given as: $E_{wf} + W_I^* E_I + W_c^* C$, where E_{wf} is the waveform misfit, E_I is the geodetic misfit, C are the constraints on the gross properties of the slip, and W_I and W_c are the relative weighting applied to the static misfit and the constraints. For the teleseismic misfit, the SH waves are generally weighted twice as much as the P waves, although a few obviously poorly fitting records are sometimes weighted less. The gross properties of the slip are constrained by minimizing the second derivative of slip between adjacent patches, and penalizing models with large moment, so that we find the smoothest slip distribution with the smallest moment that explains the data [e.g., *Hartzell and Heaton*, 1983; *Hartzell et al.*, 1996]. We explore different values of W_I and W_c.

[64] We run each teleseismic inversion several times with different dips for the fault plane and depths for the hypocenter and choose the dip and depth that best match the main pulses of the waveforms at all azimuths (which we cite in the text). In general, we find the teleseismic data are more sensitive to the dip and depth of the fault plane than the geodetic data [*Pritchard et al.*, 2006]. On the basis of the variation in fit to the waveforms, the dip can be resolved within 2–3° and the depth within about 5 km. However, all of these results are made using a one-dimensional crustal velocity model and considering that three-dimensional effects are important, any attempt to completely match the waveforms or the geodetic data is overfitting the data.

[65] **Acknowledgments.** We thank H. Nakagawa for assistance in processing the JERS data; E. Fielding, E. Price, V. Wolf, and G. Peltzer for helping us find and process the RADARSAT data; T. Melbourne for his processed Arequipa GPS data; M. Giovanni for the relocated aftershocks for the 2001 earthquake; and A. Rodriguez-Marek, J.-P. Ampuero, and R. Allmendinger for discussions. P. Lundgren and Associate Editor S. Cohen provided helpful critical reviews. This study used ERS SAR imagery acquired under a category 1 research project from the European Space Agency. JERS SAR data were provided by the Remote Sensing Technology Center of Japan through research user PAR. RADARSAT SAR data were provided by the Alaska SAR Facility. The GMT program [*Wessel and Smith*, 1998] was used to create several figures. T.H.D. and E.O.N. acknowledge support of NSF grant EAR 0003621; and M.E.P.'s contribution was funded by NSF grant EAR 0510719.

References

Beck, S. L., and L. J. Ruff (1984), The rupture process of the great 1979 Colombia earthquake: Evidence from the asperity model, *J. Geophys. Res.*, *89*, 9281–9291.

Beck, S. L., and L. J. Ruff (1989), Great earthquakes and subduction along the Peru trench, *Phys. Earth Planet. Inter.*, *57*, 199–224.

Beck, S. L., S. Barrientos, E. Kausel, and M. Reyes (1998), Source characteristics of historic earthquakes along the central Chile subduction zone, *J. South Am. Earth Sci.*, *11*, 115–129.

Benioff, H., F. Press, and S. W. Smith (1961), Excitation of free oscillations of Earth by earthquakes, *J. Geophys. Res.*, *66*, 605–619.

Bilek, S. L., and L. J. Ruff (2002), Analysis of the 23 June 2001 M_w = 8.4 Peru underthrusting earthquake and its aftershocks, *Geophys. Res. Lett.*, *29*(20), 1960, doi:10.1029/2002GL015543.

Boroschek, R., P. Soto, and R. Leon (2001), *Registros en el norte de Chile, terremoto del sur del Peru, 23 de Junio 2001, M_w = 8.4, Red Nacional de Acelerografos*, *RENADIC* (in Spanish), vol. 01/04, 35 pp., Dep. de Ing. Civ., Univ. de Chile, Santiago.

Butler, R., et al. (2004), The Global Seismographic Network surpasses its design goal, *Eos Trans. AGU*, *85*(23), 225.

Campos, J., and E. Kausel (1990), The large 1939 intraplate earthquake of southern Chile, *Seismol. Res. Lett.*, *611*, 43.

Carlo, D. L., T. Lay, C. J. Ammon, and J. Zhang (1999), Rupture process of the 1995 Antofagasta subduction earthquake (M_w = 8.1), *Pure Appl. Geophys.*, *154*, 677–709.

Choy, G. L., and J. W. Dewey (1988), Rupture process of an extended earthquake sequence: Teleseismic analysis of the Chilean earthquake of March 3, 1985, *J. Geophys. Res.*, *93*, 1103–1118.

Comte, D., and M. Pardo (1991), Reappraisal of great historical earthquakes in the northern Chile and southern Peru seismic gaps, *Nat. Hazards*, *4*, 23–44.

Farr, T. G., and M. Kobrick (2000), Shuttle Radar Topography Mission produces a wealth of data, *Eos Trans. AGU*, *81*(48), 583.

Fujiwara, S., T. Nishimura, M. Murakami, H. Nakagawa, M. Tobita, and P. Rosen (2000), 2.5-D surface deformation of *M*6.1 earthquake near Mt Iwate detected by SAR interferometry, *Geophys. Res. Lett.*, *27*, 2049–2052.

Giovanni, M. K., S. L. Beck, and L. Wagner (2002), The June 23, 2001 Peru earthquake and the southern Peru subduction zone, *Geophys. Res. Lett.*, *29*(21), 2018, doi:10.1029/2002GL015774.

Grange, F., P. Cunningham, J. Gagnepain, D. Natzfeld, P. Molnar, L. Ocola, A. Rodrigues, S. W. Roecker, J. M. Stock, and G. Suarez (1984), The configuration of the seismic zone and the downgoing slab in southern Peru, *Geophys. Res. Lett.*, *11*, 38–41.

Hartzell, S. H., and T. H. Heaton (1983), Inversion of strong ground motion and teleseismic waveform data for the fault rupture history of the 1979 Imperial Valley, California, earthquake, *Bull. Seismol. Soc. Am.*, *73*, 1553–1583.

Hartzell, S. H., and C. Langer (1993), Importance of model parameterization in finite fault inversions: Application to the 1974 M_w 8.0 Peru earthquake, *J. Geophys. Res.*, *98*, 22,123–22,134.

Hartzell, S. H., P. Liu, and C. Mendoza (1996), The 1994 Northridge, California earthquake: Investigation of rupture velocity, risetime, and high-frequency radiation, *J. Geophys. Res.*, *101*, 20,091–20,108.

Hasegawa, A., and S. Sacks (1981), Subduction of the Nazca plate beneath Peru as determined from seismic observations, *J. Geophys. Res.*, *86*, 4971–4980.

Heflin, M., et al. (1992), Global geodesy using GPS without fiducial sites, *Geophys. Res. Lett.*, *19*, 131–134.

Hjorleifsdottir, V., C. Ji, T. A. Song, Q. Liu, J. Tromp, and H. Kanamori (2005), Very broad-band modeling of the Dec. 26th, 2004, Sumatra-Andaman earthquake (abstract), *Eos Trans. AGU*, *86*(52), Fall Meet. Suppl., Abstract U21C-05.

Husen, S., E. Kissling, E. Flueh, and G. Asch (1999), Accurate hypocentre determination in the seismogenic zone of the subducting Nazca Plate in northern Chile using a combined on-/offshore network, *Geophys. J. Int.*, *138*, 687–701.

Ihmlé, P. F., and R. Madariaga (1996), Monochromatic body waves excited by great subduction zone earthquakes, *Geophys. Res. Lett.*, *23*, 2999–3002.

Ihmlé, P. F., J.-M. Gomez, P. P. Heinrich, and S. Guibourg (1998), The 1996 Peru tsunamigenic earthquake: Broadband source process, *Geophys. Res. Lett.*, *25*, 2691–2694.

Ji, C., D. J. Wald, and D. V. Helmberger (2002), Source description of the 1999 Hector Mine, California, earthquake, part I: Wavelet domain inversion theory and resolution analysis, *Bull. Seismol. Soc. Am.*, *92*, 1192–1207.

Kanamori, H., and J. Given (1981), Use of long-period surface waves for rapid determination of earthquake-source parameters, *Phys. Earth Planet. Inter.*, *27*, 8–36.

Kelleher, J. A. (1972), Rupture zones of large South American earthquakes and some predictions, *J. Geophys. Res.*, *77*, 2087–2103.

Kikuchi, M., and Y. Yamanaka (2001), Earthquake information center, (*Seismol. Note 105*, Univ. of Tokyo, Tokyo. (Available at http://wwweic.eri.u-tokyo.ac.jp/EIC/EIC_News/105E.html)

Langer, C. J., and W. Spence (1995), The 1974 Peru earthquake series, *Bull. Seismol. Soc. Am.*, *85*, 665–687.

Lay, T., and T. C. Wallace (1995), *Modern Global Seismology*, Elsevier, New York.

Lay, T., et al. (2005), The great Sumatra-Andaman earthquake of 26 December 2004, *Science*, *308*, 1127–1133.

Ludwig, W. J., J. E. Nafe, and C. L. Drake (1970), Seismic refraction, in *The Sea*, vol. 4, edited by A. E. Maxwell, pp. 53–84, John Wiley, Hoboken, N. J.

Manga, M. (2001), Origin of postseismic streamflow changes inferred from baseflow recession and magnitude-distance relations, *Geophys. Res. Lett.*, *28*, 2133–2136.

Manga, M., E. E. Brodsky, and M. Boone (2003), Response of streamflow to multiple earthquakes and implications for the origin of postseismic discharge changes, *Geophys. Res. Lett.*, *30*(5), 1214, doi:10.1029/2002GL016618.

Massonnet, D., and K. Feigl (1998), Radar interferometry and its application to changes in the Earth's surface, *Rev. Geophys.*, *36*, 441–500.

Massonnet, D., K. L. Feigl, H. Vadon, and M. Rossi (1996), Coseismic deformation field of the M = 6.7 Northridge, California earthquake of January 17. 1994 recorded by two radar satellites using interferometry, *Geophys. Res. Lett.*, *23*, 969–972.

McGuire, J. J., L. Zhao, and T. H. Jordan (2002), Predominance of unilateral rupture for a global catalog of large earthquakes, *Bull. Seismol. Soc. Am.*, *92*, 3309–3317.

Melbourne, T. I., and F. H. Webb (2002), Precursory transient slip during the 2001 M_w = 8.4 Peru earthquake sequence from continuous GPS, *Geophys. Res. Lett.*, *29*(21), 2032, doi:10.1029/2002GL015533.

Melbourne, T., F. Webb, J. Stock, and C. Reigber (2002), Rapid postseismic transients in subduction zones from continuous GPS, *J. Geophys. Res.*, *107*(B10), 2241, doi:10.1029/2001JB000555.

Mendoza, C., S. Hartzell, and T. Monfret (1994), Wide-band analysis of the 3 March 1985 central Chile earthquake – overall source process and rupture history, *Bull. Seismol. Soc. Am.*, *84*, 269–283.

Michel, R., J.-P. Avouac, and J. Taboury (1999), Measuring ground displacements from SAR amplitude images: Application to the Landers earthquake, *Geophys. Res. Lett.*, *26*, 875–878.

Murakami, M., M. Tobita, S. Fujiwara, T. Saito, and H. Masaharu (1996), Coseismic crustal deformations of 1994 Northridge, California, earthquake detected by interferometric JERS 1 synthetic aperture radar, *J. Geophys. Res.*, *101*, 8605–8614.

Norabuena, E., L. Leffler-Griffin, A. Mao, T. H. Dixon, S. Stein, I. S. Sacks, L. Ocola, and M. Ellis (1998), Space geodetic observations of Nazca-South America convergence across the central Andes, *Science*, *279*, 358–361.

Norabuena, E., T. H. Dixon, S. Stein, and C. G. A. Harrison (1999), Decelerating Nazca-South America and Nazca-Pacific plate notions, *Geophys. Res. Lett.*, *26*, 3405–3408.

Norabuena, E. O. (2004), Space geodetic studies of crustal deformation in subduction zones: The central Andes and Costa Rica, Ph.D. thesis, Univ. of Miami, Miami, Fla.

Ozawa, S., M. Murakami, S. Fujiwara, and M. Tobita (1997), Synthetic aperture radar interferogram of the 1995 Kobe earthquake and its geodetic inversion, *Geophys. Res. Lett.*, *24*, 2327–2330.

Pelayo, A. M., and D. A. Wiens (1990), The November 20, 1960 Peru tsunami earthquake: Source mechanism of a slow event, *Geophys. Res. Lett.*, *17*, 661–664.

Peltzer, G., F. Cramp, and G. King (1999), Evidence of nonlinear elasticity of the crust from the M_w 7.6 Manyi (Tibet) earthquake, *Science*, *286*, 272–276.

Pritchard, M. E. (2003), Recent crustal deformation in west-central South America, Ph.D. thesis, Calif. Inst. of Technol., Pasadena.

Pritchard, M. E., and M. Simons (2004), An InSAR-based survey of volcanic deformation in the central Andes, *Geochem. Geophys. Geosys.*, *5*, Q02002, doi:10.1029/2003GC000610.

Pritchard, M. E., M. Simons, P. Rosen, S. Hensley, and F. Webb (2002), Coseismic slip from the 1995 July 30 M_w = 8.1 Antofagasta, Chile, earthquake as constrained by InSAR and GPS observations, *Geophys. J. Int.*, *150*, 362–376.

Pritchard, M. E., C. Ji, and M. Simons (2006), Distribution of slip from 11 $M_w > 6$ earthquakes in the northern Chile subduction zone, *J. Geophys. Res.*, *111*, B10302, doi:10.1029/2005JB004013.

Robinson, D. P., S. Das, and A. B. Watts (2006), Earthquake rupture stalled by a subducting fracture zone, *Science*, *312*, 1203–1205.

Rodriguez-Marek, A., J. L. Williams, J. Wartman, P. C. Repetto, E. Rondinel, J. Zegarra-Pellane, and D. M. Baures (2003), Ground motion and site response, *Earthquake Spectra*, *19*, 11–34, *Suppl. A*.

Rosen, P. A., S. Hensley, H. A. Zebker, F. H. Webb, and E. J. Fielding (1996), Surface deformation and coherence measurements of Kilauea Volcano, Hawaii, from SIR-C radar interferometry, *J. Geophys. Res.*, *101*, 23,109–23,125.

Rosen, P. A., S. Hensley, I. R. Joughin, F. K. Li, S. N. Madsen, E. Rodríguez, and R. M. Goldstein (2000), Synthetic Aperture Radar Interferometry, *Proc. IEEE*, *88*, 333–382.

Rosen, P. A., S. Hensley, G. Peltzer, and M. Simons (2004), Updated Repeat Orbit Interferometry Package released, *Eos Trans. AGU*, *85*(5), 47.

Rothman, D. H. (1986), Automatic estimation of large residual statics corrections, *Geophysics*, *51*, 337–346.

Rubin, A. M., and D. Gillard (2000), Aftershock asymmetry/rupture directivity among central San Andreas fault microearthquakes, *J. Geophys. Res.*, *105*, 19,095–19,109.

Ruegg, J. C., M. Olcay, and D. Lazo (2001), Co-, post- and pre (?)-seismic displacements associated with the M_w = 8.4 southern Peru earthquake of 23 June 2001 from continuous GPS measurements, *Seismol. Res. Lett.*, *72*, 673–678.

Salichon, J., B. Delouis, P. Lundgren, D. Giardini, M. Constantini, and P. Rosen (2003), Joint inversion of broadband teleseismic and interferometric synthetic aperture radar (InSAR) data for the slip history of the M_w = 7.7, Nazca Ridge (Peru) earthquake of 12 November 1996, *J. Geophys. Res.*, *108*(B2), 2085, doi:10.1029/2001JB000913.

Schmitz, M., W.-D. Heinsohn, and F. R. Schilling (1997), Seismic, gravity and petrological evidence for partial melt beneath the thickened central Andean crust (21–23°S), *Tectonophysics*, *205*, 127–140.

Schweller, W. J., L. D. Kulm, and R. A. Prince (1981), Tectonics, structure, and sedimentary framework of the Peru-Chile trench, *Mem. Geol. Soc. Am.*, *154*, 323–349.

Segall, P., and J. L. Davis (1997), GPS applications for geodynamics and earthquake studies, *Annu. Rev. Earth Planet. Sci.*, *25*, 301–336.

Shakal, A. F., M. J. Huang, and V. M. Grazier (1986), Strong-motion data processing, in *International Handbook of Earthquake and Engineering Seismology*, vol. B, edited by W. H. K. Lee, H. Kanamori, P. C. Jennings, and C. Kisslinger, pp. 967–981, Elsevier, New York.

Simons, M., Y. Fialko, and L. Rivera (2002), Coseismic deformation from the 1999 M_w 7.1 Hector Mine, California, earthquake as inferred from InSAR and GPS observations, *Bull. Seismol. Soc. Am.*, *92*, 1390–1402.

Spence, W., C. Mendoza, E. R. Engdahl, G. L. Choy, and E. Norabuena (1999), Seismic subduction of the Nazca Ridge as shown by the 1996–97 Peru earthquakes, *Pure Appl. Geophys.*, *154*, 753–776.

Swenson, J. L., and S. L. Beck (1996), Historical 1942 Ecuador and 1 942 Peru subduction earthquakes, and earthquake cycles along Colombia-Ecuador and Peru subduction segments, *Pure Appl. Geophys.*, *146*, 67–101.

Swenson, J. L., and S. L. Beck (1999), Source characteristics of the 12 November 1996 M_w 7.7 Peru subduction zone earthquake, *Pure Appl. Geophys.*, *154*, 731–751.

Tavera, H. (Ed.) (2002), *El terremoto de la region sur de Peru del 23 de Junio de 2001* (in Spanish), Ins. Geofis. del Peru, Lima. (Available at http://www.igp.gob.pe/cns/-reportes/2002/sis_230602_areq/_ind_sis_areq.htm.

Tavera, H., and Y. Antayhua (2002), Parámetros del terremoto de Arequipa del 23 de Junio de 2001 y de tres réplicas de magnitud mayor deducidos del análysis espectral de ondas de volumen, in *El Terremoto de la Region sur de Peru del 23 de Junio de 2001* (in Spanish), edited by H. Tavera, pp. 99–104, Ins. Geofis. del Peru, Lima.

Tavera, H., and H. Salas (2002), Algunas notas sobre las acceleraciones máximas producidas por el terremoto de Arequipa del 23 de Junio de 2001, in *El Terremoto de la Region sur de Peru del 23 de Junio de 2001* (in Spanish), edited by H. Tavera, pp. 105–110, Ins. Geofis. del Peru, Lima.

Tobita, M., S. Fujiwara, S. Ozawa, P. Rosen, E. Fielding, C. Werner, M. Murakami, H. Nakagawa, and K. Nitta (1998), Deformation of the 1995 North Sakhalin earthquake detected by JERS-1 SAR interferometry, *Earth Planets Space*, *50*, 313–325.

Wald, D. J., T. H. Heaton, and K. W. Hudnut (1996), The slip history of the 1994 Northridge, California, earthquake determined from strong-motion, teleseismic, GPS, and leveling data, *Bull. Seismol. Soc. Am.*, *86*, S49–S70.

Wessel, P., and W. H. F. Smith (1998), New, improved version of Generic Mapping Tools released, *Eos*, *79*, 579.

Wollard, G. P. (1975), Interrelationships of crustal and upper mantle parameter values in the Pacific, *Rev. Geophys.*, *13*, 87–137.

Zumberge, J. F., M. B. Heflin, D. C. Jefferson, M. M. Watkins, and F. H. Webb (1997), Precise point positioning for the efficient and robust analysis of GPS data from large networks, *J. Geophys. Res.*, *102*, 5005–5017.

R. Boroschek, Departamento de Ingenieria Civil, Universidad de Chile, Avda. Blanco Encalada 2002 4to Piso, Santiago, Chile.

D. Comte, Departamento de Geofisica, Universidad de Chile, Avenida Blanco Encalada 2002, Santiago, 651-1227, Chile.

T. H. Dixon, University of Miami, RSMAS-MGG, 4600 Rickenbacker Causeway, Miami, FL 33149, USA.

C. Ji, Department of Geological Sciences, University of California, Santa Barbara, CA 93106, USA.

E. O. Norabuena, Departamento de Geodesia y Sismotectonica, Instituto Geofisico del Peru, Calle Badajoz 169, Urb. Mayorazgo-4Etapa, Lima 3, Peru.

M. E. Pritchard, Department of Earth and Atmospheric Sciences, Cornell University, Snee Hall, Ithaca, NY 14853, USA. (mp337@cornell.edu)

P. A. Rosen, Jet Propulsion Laboratory, California Institute of Technology, 4800 Oak Grove Drive, MS 300-235, Pasadena, CA 91109-8099, USA.

M. Simons, Seismological Laboratory, Division of Geological and Planetary Sciences, California Institute of Technology, MC 252-21, Pasadena, CA 91125, USA.